

Mohamed Khider University of Biskra Faculty of exact sciences Material sciences department

MASTER DISSERTATION

Material sciences Physics Energetic Physics and Renewable Energies

Ref.:

Presented by Ben amiour Imane

On:03/06/2025

Study of MoS₂ based solar cells by simulation using SILVACO TCAD

Jury:

Abdeslam Nora Amele MCB University of Biskra President

Boumaraf Rami MCB University of Biskra Supervisor

Adel Daoud MCB University of Biskra Examiner

Academic Year: 2024/2025

Dedications

To my beloved late father, whose unwavering support guided me through every step of my life and academic path.

To my mother, who was my greatest support with her prayers, kindness, love, and constant encouragement.

To my dear sisters and my little brother, whose love and support have always meant the world to me.

Acknowledgments

I praise Allah, by whose grace this work has been completed. All thanks be to Him for His guidance and facilitation throughout my academic journey — for there is no success except by the grace of Allah.

After the grace of Allah, the greatest credit for the completion of this work goes to my supervisor, i would like to express my deepest and sincerest gratitude to **Dr.Boumaraf Rami** whose guidance, support, and insightful advice were invaluable throughout every stage of this thesis. I am truly grateful for the time and effort he devoted to reviewing my work, offering constructive feedback, and always being available to help me overcome challenges. This work would not have been possible without his mentorship.

I would also like to express my sincere gratitude to the esteemed members of the examination committee: **Dr.Abdeslam Nora Amele** and **Dr.Adel Daoud** for dedicating their time to reading and evaluating this thesis.

I am deeply grateful to my favorite professor **Pr.Meftah Afak** for generously providing me with the LaTeX template, which was of great help to me.

I would like to extend my heartfelt thanks to my family, especially my beloved mother, to my sisters and my younger brother, they were a true source of strength and inspiration throughout every stage of this journey. I would also like to sincerely thank my dear friends, whose presence, encouragement, and shared moments of stress, laughter, and motivation made this experience not only bearable but unforgettable specially my BFF "Brahmi Douaa".

This thesis would not have been possible without all of you. Thank you.

ABSTRACT

This thesis investigates the potential of molybdenum disulfide (MoS_2) as an active material for next-generation solar cells. As a two-dimensional transition metal dichalcogenide, MoS_2 exhibits exceptional optoelectronic properties, making it a strong candidate for thin-film photovoltaic applications.

The MoS_2/InP heterojunction solar cell performance is simulated and analyzed using SILVACO TCAD tools, focusing on the influence of doping concentration and thickness of the MoS_2 emitter and InP absorber layers, as well as the work functions of the front and back contacts. Simulation results identify the optimal InP absorber thickness as 2500 µm with a doping concentration of 10^{14} cm⁻³, while the MoS_2 emitter achieves best performance at a monolayer thickness (0.72 nm) and a doping density of $2.5 * 10^{20}$ cm⁻³. The front and back contact work functions are optimized at 3.7 eV and 5.65 eV, respectively. These parameters collectively enhance junction quality, charge separation, and carrier collection, resulting in a device with a V oc of 0.8627 V, J_{sc} of 24.191 mA/cm², fill factor of 85.86%, and a power conversion efficiency of 17.92%.

These findings support the use of MoS_2 as a cost-effective, flexible alternative to conventional materials, and offer promising insight into the development of high-efficiency hybrid solar cells that integrate two-dimensional and three-dimensional materials.

Keywords: Molybdenum disulfide (MoS2), Two-dimensional materials, SILVACO TCAD, Simulation, Solar cell.

ملخص

تتناول هذه المذكرة البحث في إمكانية استخدام ثاني كبريتيد الموليبدينوم (MoS_2) كمادة فعالة في خلايا الطاقة الشمسية من الجيل الجديد. يعد (MoS_2) ، باعتباره ثنائي الأبعاد ومن فئة كالكوجينيدات المعادن الانتقالية، مادةً واعدة لتطبيقات الخلايا الشمسية الرقيقة بفضل خصائصه الفريدة في مجال البصريات والإلكترونيات.

تمت محاكاة أداء خلية شمسية غير متجانسة (MoS_2/InP) و تحليلها باستخدام أدوات تمت محاكاة أداء خلية شمسية غير متجانسة (Doping) و (Doping) مع التركيز على تأثير تركيز التطعيم (MoS_2) وسمُك طبقتي باعث (MoS_2) وممتص (InP) بالإضافة إلى دالة العمل (InP) هو (InP) للاتصالين الأمامي والخلفي. أظهرت نتائج المحاكاة أن السُمك المثالي لطبقة (InP) هو (InP) هو (InP) بينما يحقق باعث (InP) أفضل أداء عند سُمك أحادي بتركيز تطعيم يبلغ (InP) بينما يحقق باعث (InP) أفضل أداء عند سُمك أحادي الطبقة (InP) نانومتر) وكثافة تطعيم تبلغ (InP) ألطبقة (InP) للاتصالين الأمامي والخلفي إلى (InP) وقد تم تحسين دالة العمل (InP) المعلمات مجتمعة في تحسين جودة الوصلة، وفصل الشحنات، وجمع الحوامل، مما يؤدي المعلمات مجتمعة في تحسين جودة الوصلة، وفصل الشحنات، وجمع الحوامل، مما يؤدي (InP) بهاز ذي جهد دائرة مفتوحة (InP) به (InP) فولت ، وكثاغة تبلغ (InP) تساوي (InP) به عامل الشكل (InP) ألله المائية الأبعاد فعالة ومنخفضة التكلفة في الخلايا الشمسية، لما تمتلكه من خصائص بصرية وإلكترونية مميزة، كما تسلط الضوء على المكانياتها الواعدة في تحسين أداء الأجهزة الكهروضوئية عند دمجها مع مواد تقليدية الأبعاد.

الكلمات المفتاحية : كبريتيد الموليبدنيوم (MoS_2) ،مواد ثنائية الابعاد،محاكاة،خلية شمسية،SILVACOTCAD.

Contents

D	Dedications				
A	Acknowledgments				
Al	bstrac	ct			iii
In	Introduction				
1	The	oretica	l Backgro	ound of Solar Cells	3
	1.1	Solar	energy: .		3
	1.2	Air m	nass		4
	1.3	Photo	voltaic sy	rstem	4
	1.4	Solar	cell's Wo	rking principle:	5
		1.4.1	Semicor	nductors:	5
			1.4.1.1	Intrinsic semiconductor:	5
			1.4.1.2	Extrinsic semiconductor:	6
		1.4.2	P-N jun	ction:	7
		1.4.3	Forward	d-biased p-n junction solar cell:	9
		1.4.4	Reverse	-biased p-n junction solar cell:	9
		1.4.5	P-N jun	ction solar cell under illumination:	9
		1.4.6	Metal-se	emiconductor junction:	10
	1.5	Solar	Cell I-V C	Characteristics:	10
		1.5.1	Short-ci	rcuit current:	11
		1.5.2	Open-ci	rcuit voltage:	11
		1.5.3	Efficience	cy:	11
		1.5.4	Fill facto	or:	12
	1.6	Photo	voltaic ce	ells development:	12
		1.6.1	First ger	neration of photovoltaic cells:	12
			1.6.1.1	Monocrystalline silicon (m-Si)-based solar cells:	12
			1.6.1.2	Polycrystalline silicon (p-si)-based solar cells:	13
			1.6.1.3	Multicrystalline silicon-based solar cells:	13

			1.6.1.4 Single III-V junction (GaAs)-based solar cells: 14	1
		1.6.2	Second generation of photovoltaic cells:	1
			1.6.2.1 Amorphous silicon-based photovoltaic cells: 14	1
			1.6.2.2 CdTe solar cells:	5
			1.6.2.3 CIGS solar cells:	5
			1.6.2.4 Kesterite solar Cells:	ó
		1.6.3	Third generation of photovoltaic cells:	ó
			1.6.3.1 Organic and polymeric materials photovoltaic cells (OSC): 1	6
			1.6.3.2 Dye-sensitized photovoltaic cells (DSSC): 16	ó
			1.6.3.3 Perovskite solar cells:	7
			1.6.3.4 Quantum dots photovoltaic cells:	7
			1.6.3.5 Multi-junction photovoltaic cells:	7
		1.6.4	Forth generation of photovoltaic cells:	7
			1.6.4.1 Graphene-Based Photovoltaic Cells:	3
2	Ove	rview (of the Materials Used)
	2.1	Mater	ials at the nanoscale)
	2.2		limensional materials)
	2.3		odenum disulfide)
		2.3.1	Cristal structure	1
		2.3.2	Properties	3
			2.3.2.1 Optical propeties	3
			2.3.2.2 Electronic properties	1
		2.3.3	MoS_2 synthesis	5
			2.3.3.1 Top-down approach	5
			2.3.3.2 Bottom-Up approach	3
		2.3.4	MoS_2 in photovoltaic applications)
	2.4	Indiur	m Phosphide	Ĺ
		2.4.1	Cristal structure	Ĺ
		2.4.2	Electrical properties	2
		2.4.3	Optical properties	1
		2.4.4	InP synthesis	1
			2.4.4.1 Liquid Encapsulated Czochralski (LEC)	5
3	Sim	ulation	and Results 37	7
	3.1		o's TCAD Software	
		3.1.1	DECKBUILD	
		3.1.2	ATLAS	
		3.1.3	TONYPLOT	
	3.2		ation by ATLAS	

CONTENTS

	3.2.1	Structure specification	39
		3.2.1.1 Mesh	39
		3.2.1.2 Region	40
		3.2.1.3 Electrodes	40
		3.2.1.4 Doping	40
	3.2.2	Materials and Models Specification	40
		3.2.2.1 Material	40
		3.2.2.2 Models	41
		3.2.2.3 Contact	41
	3.2.3	Numerical Methods Selection	41
	3.2.4	Solution Specification	42
		3.2.4.1 "LOG"	42
		3.2.4.2 "SOLVE"	42
		3.2.4.3 "LOAD" and "SAVE"	42
	3.2.5	Extraction and Plotting data	43
3.3	Result	s and Discussion	43
	3.3.1	Effect of Absorber Layer Doping Concentration	44
	3.3.2	Effect of Emitter Layer Doping Concentration	46
	3.3.3	Effect of Absorber layer thickness	47
	3.3.4	Effect of Emitter layer thickness	49
	3.3.5	Impact of Back Contact Work Function	51
	3.3.6	Impact of Front Contact Work Function	53
3.4	Final l	Results	54
Conclu	sion		55
Bibliog	raphv		58

List of Figures

1.1	The photovoltaic process: photons Absorption (A), carriers Generation	
	(G), carriers Collection (C) [13]	5
1.2	Band model for an n-type semiconductor [17]	7
1.3	Band model for a p-type semiconductor [17]	8
1.4	N-type semiconductor [15]	8
1.5	P-type semiconductor [15]	8
1.6	P-n junction at equilibrium [19]	8
1.7	Band diagrams of metal-semiconductor junction [17]	10
1.8	I-V characteristic curve of a solar cell [26]	11
1.9	Development in photovoltaic cell technologies [29]	13
1.10	Schematic representation of: (a) the Czochralski process for producing	
	monocrystalline blocks and (b) the directional solidification process for	
	creating multicrystalline blocks [29]	14
1.11	Demonstration of the CIGS-based solar cell [29]	15
2.1	Schematic depiction of 2D materials and their properties [37]	21
2.2	Various coordination and stacking arrangements of the three MoS_2 struc-	
	tures: 1T, 2H, and 3R [40]	22
2.3	The crystal structure of MoS_2 [43]	23
2.4	The absorption coefficient of mono-layer MoS_2 [45]	24
2.5	The refractive index of mono-layer MoS_2 [45]	25
2.6	The calculated projected density of states (PDOS) for both bulk and	
	monolayer MoS_2 are presented for Mo(4d) and S(3p) states. The leg-	
	ends for the p- and d-orbitals are the same for both the monolayer and	
	bulk forms [46]	26
2.7	Various methods for synthesizing MoS_2 [47]	27
2.8	Schematic representation of the mechanical milling process for produc-	
	MoS_2 sheets [48]	27
2.9	The process of synthesizing a 2D MoS_2 film on conventional insulating	
	substrates using the PVD method [49]	29
	<u>♥</u>	

2.10	(a) A diagram depicting the three-zone CVD growth chamber.(b) The temperature program applied during the synthesis of monolayer MoS_2 .(c)	
	A schematic showing the MoS_2 growth on a sapphire substrate [47]	29
2.11	(a) Schematic illustration of the MoS_2 thin film synthesis on a glass/FTO	
	substrate using the microwave-assisted method, (b) Camera image show-	
	ing the MoS_2 thin film on the glass/FTO substrate alongside a bare	
	glass/FTO substrate, (c) High-resolution FESEM image of the synthe-	
	sized thin MoS_2 film, (d) Raman spectrum of the MoS_2 thin film show-	
	ing the E1 2g and A1g vibrational modes peaks [39]	30
2.12	Unit cell crystal structure of indium phosphide shown in: (a) front view	
	and (b) general view [59]	32
2.13	The two crystalline forms of InP: (a) Wurtzite (WZ) and (b) Zinc blende	
	(ZB) [61]	33
2.14	Electronic band structure of InP, referenced to the Fermi level (set to zero	
	energy) [64]	33
2.15	Refractive index of Indium Phosphide (InP) [66]	34
2.16	The absorption coefficient of Indium Phosphide (InP) [66]	35
2.17	Diagram illustrating the furnace for the Liquid Encapsulated Czochral-	
	ski method [69]	36
3.1	The simulated structure of the MoS_2/InP solar cell	44
J.1		
3.2	Variation of the JV Curve with InP Doping Concentration	45
3.2 3.3	Variation of the JV Curve with InP Doping Concentration Solar cell parameters as a function of InP doping concentration	45 45
3.2 3.3 3.4	Variation of the JV Curve with InP Doping Concentration Solar cell parameters as a function of InP doping concentration Variation of the JV Curve with MoS_2 doping concentration	45 45 46
3.2 3.3 3.4 3.5	Variation of the JV Curve with InP Doping Concentration Solar cell parameters as a function of InP doping concentration Variation of the JV Curve with MoS_2 doping concentration Solar cell parameters as a function of MoS_2 doping concentration	45 45
3.2 3.3 3.4	Variation of the JV Curve with InP Doping Concentration Solar cell parameters as a function of InP doping concentration Variation of the JV Curve with MoS_2 doping concentration Solar cell parameters as a function of MoS_2 doping concentration Energy band diagrams of MoS_2 under different donor doping concentration.	45 45 46
3.2 3.3 3.4 3.5	Variation of the JV Curve with InP Doping Concentration Solar cell parameters as a function of InP doping concentration Variation of the JV Curve with MoS_2 doping concentration Solar cell parameters as a function of MoS_2 doping concentration Energy band diagrams of MoS_2 under different donor doping concentrations: (a) and (b) show the full spatial profiles for low and high donor	45 45 46
3.2 3.3 3.4 3.5	Variation of the JV Curve with InP Doping Concentration Solar cell parameters as a function of InP doping concentration Variation of the JV Curve with MoS_2 doping concentration Solar cell parameters as a function of MoS_2 doping concentration Energy band diagrams of MoS_2 under different donor doping concentrations: (a) and (b) show the full spatial profiles for low and high donor doping, respectively. Insets (c) and (d) provide zoomed-in views near	45 45 46 47
3.2 3.3 3.4 3.5	Variation of the JV Curve with InP Doping Concentration Solar cell parameters as a function of InP doping concentration Variation of the JV Curve with MoS_2 doping concentration Solar cell parameters as a function of MoS_2 doping concentration Energy band diagrams of MoS_2 under different donor doping concentrations: (a) and (b) show the full spatial profiles for low and high donor doping, respectively. Insets (c) and (d) provide zoomed-in views near the surface	45 45 46
3.2 3.3 3.4 3.5 3.6	Variation of the JV Curve with InP Doping Concentration Solar cell parameters as a function of InP doping concentration Variation of the JV Curve with MoS_2 doping concentration Solar cell parameters as a function of MoS_2 doping concentration Energy band diagrams of MoS_2 under different donor doping concentrations: (a) and (b) show the full spatial profiles for low and high donor doping, respectively. Insets (c) and (d) provide zoomed-in views near the surface	45 45 46 47 48
3.2 3.3 3.4 3.5 3.6	Variation of the JV Curve with InP Doping Concentration Solar cell parameters as a function of InP doping concentration Variation of the JV Curve with MoS_2 doping concentration Solar cell parameters as a function of MoS_2 doping concentration Energy band diagrams of MoS_2 under different donor doping concentrations: (a) and (b) show the full spatial profiles for low and high donor doping, respectively. Insets (c) and (d) provide zoomed-in views near the surface	45 45 46 47 48 48
3.2 3.3 3.4 3.5 3.6 3.7 3.8	Variation of the JV Curve with InP Doping Concentration Solar cell parameters as a function of InP doping concentration Variation of the JV Curve with MoS_2 doping concentration Solar cell parameters as a function of MoS_2 doping concentration Energy band diagrams of MoS_2 under different donor doping concentrations: (a) and (b) show the full spatial profiles for low and high donor doping, respectively. Insets (c) and (d) provide zoomed-in views near the surface	45 45 46 47 48 48 49
3.2 3.3 3.4 3.5 3.6 3.7 3.8 3.9 3.10	Variation of the JV Curve with InP Doping Concentration Solar cell parameters as a function of InP doping concentration Variation of the JV Curve with MoS_2 doping concentration Solar cell parameters as a function of MoS_2 doping concentration Energy band diagrams of MoS_2 under different donor doping concentrations: (a) and (b) show the full spatial profiles for low and high donor doping, respectively. Insets (c) and (d) provide zoomed-in views near the surface	45 45 46 47 48 48 49 50
3.2 3.3 3.4 3.5 3.6 3.7 3.8 3.9 3.10	Variation of the JV Curve with InP Doping Concentration Solar cell parameters as a function of InP doping concentration Variation of the JV Curve with MoS_2 doping concentration Solar cell parameters as a function of MoS_2 doping concentration Energy band diagrams of MoS_2 under different donor doping concentrations: (a) and (b) show the full spatial profiles for low and high donor doping, respectively. Insets (c) and (d) provide zoomed-in views near the surface	45 45 46 47 48 48 49 50
3.2 3.3 3.4 3.5 3.6 3.7 3.8 3.9 3.10 3.11	Variation of the JV Curve with InP Doping Concentration Solar cell parameters as a function of InP doping concentration	45 46 47 48 48 49 50 50
3.2 3.3 3.4 3.5 3.6 3.7 3.8 3.9 3.10 3.11	Variation of the JV Curve with InP Doping Concentration Solar cell parameters as a function of InP doping concentration Variation of the JV Curve with MoS_2 doping concentration Solar cell parameters as a function of MoS_2 doping concentration Energy band diagrams of MoS_2 under different donor doping concentrations: (a) and (b) show the full spatial profiles for low and high donor doping, respectively. Insets (c) and (d) provide zoomed-in views near the surface	45 46 47 48 48 49 50 50
3.2 3.3 3.4 3.5 3.6 3.7 3.8 3.9 3.10 3.11 3.12 3.13	Variation of the JV Curve with InP Doping Concentration Solar cell parameters as a function of InP doping concentration	45 46 47 48 48 49 50 51 52

T	TCT	OF	CI	CI	ID.	CC
	151	() H	HI	(-1	JK	\vdash

3.16	J-V	characteristic of The optimized cell.	 5
	,		

List of Tables

2.1	Applications of MoS_2 in solar cells [54]	31
3.1	Input parameters of the Materials Used	43
3.2	MoS_2 properties depending on the number of layers	50
3.3	Best obtained performance	55

Introduction

For a long time, humanity has relied on various conventional energy sources such as fossil fuels, coal, natural gas, and agricultural waste. However, the prolonged use of these resources has led to significant environmental issues, including air and water pollution, and harm to wildlife. Problems such as global warming, acid rain, and soil degradation are direct consequences of depending on these traditional energy sources. Moreover, the finite nature of these resources and their environmental impact have driven the shift toward clean and sustainable alternatives, known as non-conventional energy sources. Options like tidal, wind, biomass, and solar energy offer renewable solutions. Among them, solar energy stands out as a particularly attractive and viable alternative to fossil fuels, as it is abundantly available across the globe [1].

Solar energy is obtained by capturing and making use of the sun's light and heat. It is an abundant resource, with the sun emitting a vast amount of energy on a daily basis. Moreover, it is renewable, meaning it can be naturally replenished over time. In contrast to fossil fuels, which require millions of years to form and are limited in quantity, solar energy is virtually inexhaustible and can be utilized as long as the sunlight is available. Photovoltaic technologies have progressed significantly, leading to improved solar cell efficiency, lower production costs, and greater adaptability across different settings. These advancements have paved the way for large-scale solar energy generation and have facilitated the incorporation of solar power into daily life [2].

Currently, crystalline silicon (c-Si) solar cells continue to lead the commercial market, thanks to the wide availability of silicon, their high efficiency, and long-term stability. Nevertheless, the advancement of these solar cells is hindered by their relatively high cost, mainly resulting from the complexity of the manufacturing process [3].

In recent years, two-dimensional transition metal dichalcogenides (TMDs), particularly molybdenum disulfide (MoS₂), have garnered significant interest for use in emerging electronic and optoelectronic devices. Compared to traditional silicon-based semiconductors, monolayer MoS₂ is seen as a promising alternative for future electronic components [4]. Among all two-dimensional TMDs, MoS₂ stands out as one of the few materials with a naturally layered structure, allowing for easy and low-cost exfoliation without complex synthesis. Additionally, its direct band gap and excellent

electrical properties make it one of the most promising 2D semiconductors, attracting significant attention in the field [5].

While 2D heterostructure devices have shown remarkable electrical properties, their power conversion efficiencies (PCEs) typically remain below 1% due to limited light absorption. In contrast, combining 2D materials with three-dimensional (3D) semiconductors shows great potential for efficient photovoltaic applications. Indium phosphide (InP), with its optimal 1.34 eV bandgap, is well-suited for solar energy conversion and offers greater resistance to space radiation compared to Si and GaAs [6].

This thesis aims to study and enhance the performance of a 2D material/3D semi-conductor heterostructure solar cell, based on the two-dimensional material molybdenum disulfide (MoS₂) combined with indium phosphide (InP), through simulation-based analysis using SILVACO TCAD tools. The work focuses on improving the power conversion efficiency (PCE) by investigating key parameters using numerical simulations—an approach that offers a more efficient and practical alternative to traditional experimental methods, which are often time-consuming and resource-intensive. Additionally, simulation studies on MoS₂-based solar cells remain relatively limited, highlighting the relevance of this work. By analyzing the effects of various design and material factors, the study seeks to uncover the underlying mechanisms that influence device performance and to propose optimization strategies that could contribute to the development of more efficient next-generation photovoltaic devices.

The dissertation is organized into three main chapters, each addressing a specific aspect of the study. Starting with a general introduction that provides background, context, and research objectives.

Chapter One presents the theoretical background, covering the fundamentals of solar cells, their operating principles, various types, as well as recent technological advancements.

Chapter Two focuses on the materials used in the device under study. It describes the physical properties of molybdenum disulfide (MoS₂) and indium phosphide (InP), highlighting their crystal structures and general characteristics.

Chapter Three introduces the SILVACO TCAD simulation environment, describing its capabilities and how it was employed to model the MoS_2/InP solar cell. This chapter presents the simulation setup, analyzes the obtained results, and discusses the effects of key parameters on device performance.

Finally, the thesis ends with a conclusion that summarizes the key findings, highlights the contributions of the study, and proposes directions for future research, including possible enhancements.

Chapter 1

Theoretical Background of Solar Cells

Sunlight is an abundant, safe, and environmentally friendly energy source capable of supporting sustainable economic development. One of the most effective and practical methods to utilize solar energy is by converting it into electricity through solar cells [7]. Solar cells , also known as photovoltaic (PV) cells, generate electricity from light using the photovoltaic effect [8].

Since their discovery, these cells have undergone significant developments in terms of efficiency, the materials used in their fabrication, and their diverse applications.

This chapter aims to provide a comprehensive overview of the working principles of solar cells, starting with the basic physics behind the photovoltaic effect, followed by an exploration of different types of solar cell technologies.

1.1 Solar energy:

Solar energy is the cleanest and most abundant form of renewable energy available. Advances in technology now allow both individuals and businesses to harness this resource in various ways, utilizing both sunlight and heat. Solar energy is directly produced by the sun, which generates energy through a thermonuclear process that converts around 650 million tons of hydrogen into helium every second. This process releases heat and electromagnetic radiation, with the heat remaining within the sun to sustain the nuclear reactions. The electromagnetic radiation, including visible light, infrared, and ultraviolet rays, radiates outward into space. Only a small fraction of this radiation reaches Earth, yet it serves as the indirect source of nearly all forms of energy on the planet, with the exceptions of geothermal energy and nuclear fission and fusion. Even fossil fuels originated from the sun, as they were once living organisms that depended on solar energy. Approximately 52 petawatts (PW) of solar radiation is reflected back into space, accounting for 30% of the total. As a result, more solar energy is available in outer space, which has led to proposals for launching photovoltaic arrays into space to collect this energy and transmit it back to Earth as microwaves for

use. At the top of the atmosphere, the solar constant provides around 1.4 kW/m² of energy. Given that global energy consumption (from oil, gas, coal, nuclear, and other sources) totals around 18 terawatts (TW), the amount of solar radiation hitting Earth is approximately 10,000 times greater. Capturing even a small portion of this energy could potentially solve the looming energy crisis [9].

1.2 Air mass

Solar radiation emitted by the sun forms the solar spectrum as detected on Earth. Above the Earth's atmosphere, the radiation intensity, known as the Solar Constant, measures around 1.353 kW/ m^2 . The spectral profile in this region is called the air mass zero (AM0) spectrum. Air Mass describes how the atmosphere modifies the solar radiation by absorbing certain wavelengths and reducing its intensity before it reaches the surface [10]. The Air Mass value is determined by the following relationship [10]:

$$AM = \frac{1}{\cos(\theta)} \tag{1.1}$$

where θ represents the angle at which sunlight strikes the surface (with $\theta = 0$ when the sun is positioned directly overhead) [10].

The air mass coefficient is commonly utilized to define the standardized testing conditions for solar cell performance. It is denoted as "AM1.5", indicating an atmospheric thickness corresponding to a solar zenith angle of 48.2°. To ensure accurate and consistent comparisons of solar cell performance across different times and locations, a standard spectrum and power density are typically applied. The designations "AM1.5G" (where G refers to global, meaning it includes both direct and diffuse sunlight) and "AM1.5D" (referring to only direct sunlight) are used to describe the standard solar spectrum at the Earth's surface [11].

1.3 Photovoltaic system

Photovoltaics (PV) is a method of generating electrical power by harnessing solar energy. PV systems employ solar panels composed of multiple photovoltaic cells, which utilize semiconductor materials to convert sunlight into direct current electricity through the photovoltaic effect [12].

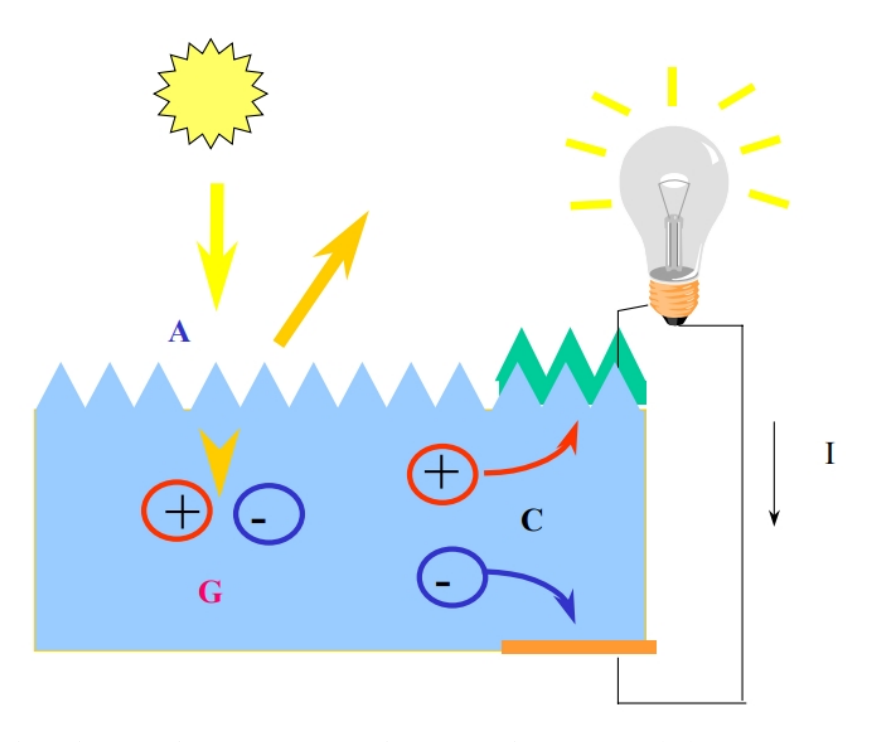


Figure 1.1: The photovoltaic process: photons Absorption (A), carriers Generation (G), carriers Collection (C) [13].

1.4 Solar cell's Working principle:

A photovoltaic (PV) cell is a semiconductor device that converts solar radiation into electrical energy. It consists of a p-n junction, formed by the interface of p-type and n-type semiconductor materials. The absorption of photons from sunlight creates electronhole pairs, which are separated by the junction, resulting in the generation of direct current (DC) electricity [14].

1.4.1 Semiconductors:

Semiconductors are primarily classified into two categories [15]:

- Intrinsic semiconductors.
- Extrinsic semiconductors.

1.4.1.1 Intrinsic semiconductor:

An intrinsic semiconductor can be defined in two ways. In simple terms, it is a semiconductor made from a very pure material. More technically, an intrinsic semiconductor is one where the number of holes (vacant electron states) equals the number of electrons in the conduction band ($n_i = n = p$) [15], where n_i is the intrinsic carrier concentration, a key semiconductor property. It's easy to see that [16]:

$$n_i^2 = n.p (1.2)$$

The concentration of electrons and holes is calculated using the following equations [16]:

$$n = N_C.exp(\frac{E_F - E_C}{KT}) \tag{1.3}$$

$$p = N_V . exp(\frac{E_V - E_F}{KT}) \tag{1.4}$$

from 1.3, 1.4 and 1.2 we get [16]:

$$n_i^2 = \sqrt{N_C N_V} . exp(\frac{-E_G}{2KT})$$
(1.5)

These semiconductors have a very small energy gap, and at room temperature, the energy available is enough to excite valence electrons into the conduction band. Another key characteristic is that the Fermi level of an intrinsic semiconductor lies between the valence and conduction bands. The Fermi level is the energy level where the probability of finding an electron is 50% (a probability of 0.5 on a scale from 0 to 1). When a potential difference is applied across an intrinsic semiconductor, electrons move toward the positive terminal, and holes move toward the negative terminal. The total current in the semiconductor is the sum of the currents due to both free electrons and holes. As the temperature increases, the number of electron-hole pairs rises, resulting in an increase in current. Conversely, when the temperature decreases, the number of electron-hole pairs decreases, and the current diminishes [15].

1.4.1.2 Extrinsic semiconductor:

These are semiconductors in which the pure form of the semiconductor material is intentionally altered by adding very small amounts of impurities. These impurities are referred to as dopants or doping agents. It is important to note that the quantity of these impurities is extremely small, with a typical dopant concentration being around 1 part per hundred million, or 0.01 ppm. The dopants are carefully selected based on the number of electrons in their valence band: pentavalent dopants have five electrons, while trivalent dopants have three. As a result, the dopant type leads to the formation of two types of extrinsic semiconductors P-type and N-type semiconductors [15].

• N-type: Consider a semiconductor to which donor-type impurities have been added (figure 1.4) . Figure 1.2 illustrates the band model for an n-type semiconductor as the temperature increases. At T=0 K, the electrons are in their valence bonds, and the donor electron, which is not part of the covalent bonds, has higher energy compared to the electrons that are bonded. The energy needed to move the donor electron to the

conduction band is much lower than the energy required to move an electron involved in covalent bonding. The energy difference between the conduction band (EC) and the donor level (ED) is very small, so even a slight increase in temperature can cause the donor electron to transition to the conduction band, resulting in ionization. In an n-type semiconductor, the Fermi level is located near the conduction band [17]. For an n-type semiconductor, assuming that N_A is null and considering that $N_D \approx n_0$, the concentration of holes can be determined by [17]:

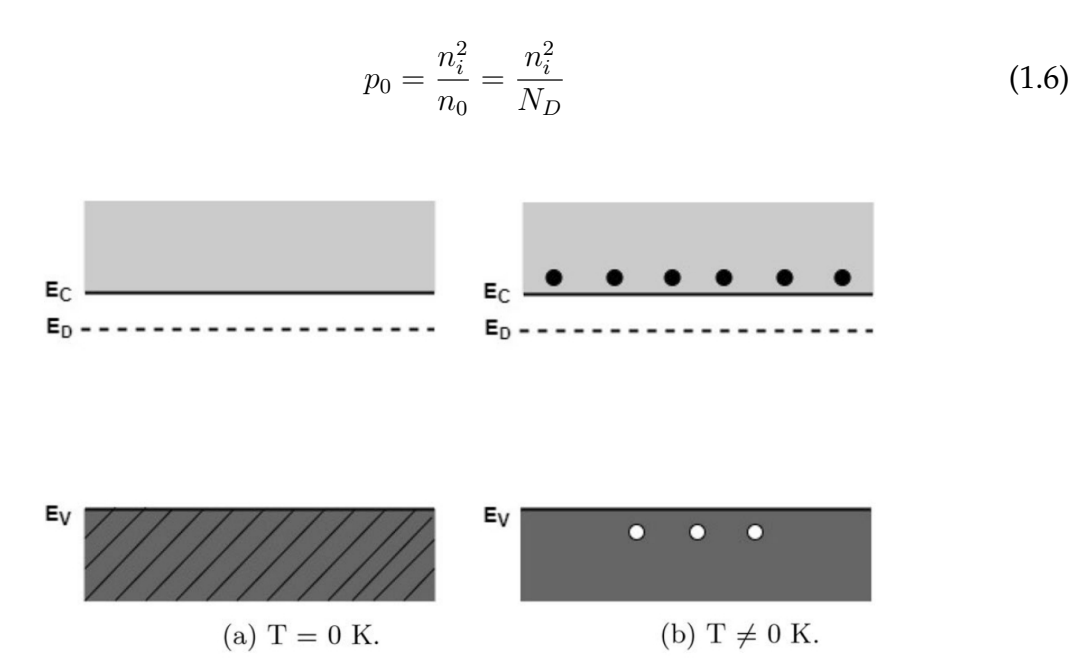


Figure 1.2: Band model for an n-type semiconductor [17].

• **P-type:** Consider a semiconductor doped with acceptor-type impurities (figure 1.5). Figure 1.3 illustrates the band structure of a p-type semiconductor as the temperature increases. At T = 0 K, the covalent bonds are incomplete, and their energy is above the valence band edge (EV). A slight increase in temperature is sufficient to excite an acceptor electron into the conduction band, ionizing the impurity. As a result, the valence band contains significantly more holes than electrons in the conduction band, as depicted in Figure 1.3 [17]. For a p-type semiconductor, assuming that ND is null and that $N_A \approx p_0$, the concentration of holes can be determined by [17]:

$$n_0 = \frac{n_i^2}{p_0} = \frac{n_i^2}{N_A} \tag{1.7}$$

1.4.2 P-N junction:

When a p-type semiconductor comes into contact with an n-type semiconductor, free electrons from the n-type region near the heterojunction will diffuse into the p-type region, as the electron concentration is significantly higher in the n-type region than

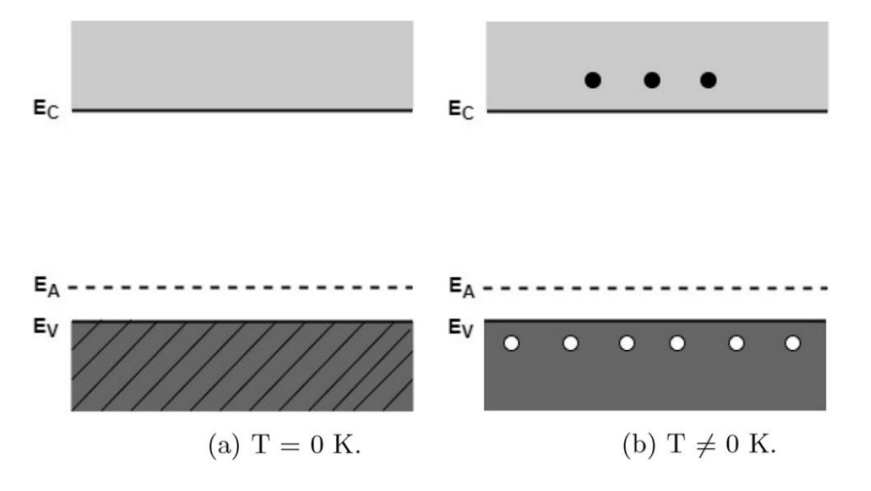


Figure 1.3: Band model for a p-type semiconductor [17].

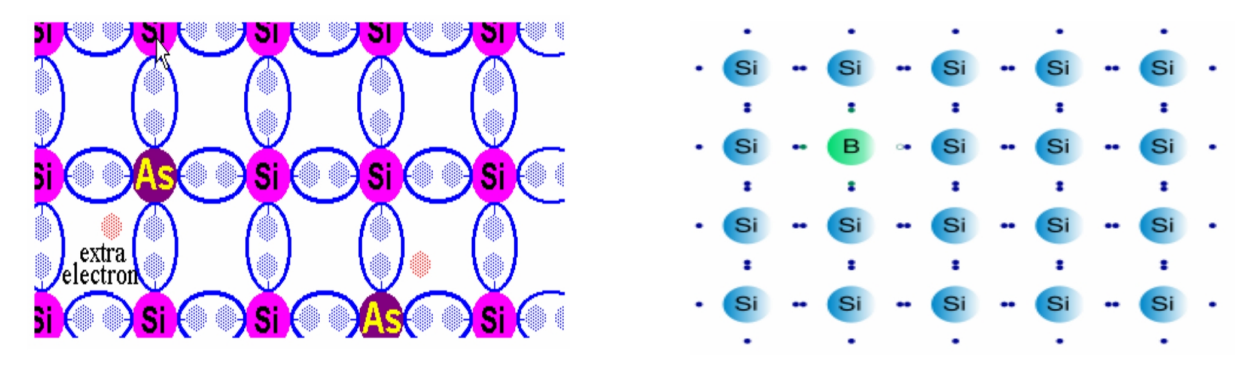


Figure 1.4: N-type semiconductor [15].

Figure 1.5: P-type semiconductor [15].

in the p-type region. As the electrons diffuse across the junction, they leave behind a layer of fixed positive charge in the n-type semiconductor. Similarly, free holes from the p-type semiconductor near the junction will diffuse into the n-type region, leaving behind a layer of negative charge in the p-type semiconductor. This separation of charges creates an electrostatic field that opposes further diffusion across the junction. Equilibrium is reached when the diffusion of majority carriers across the junction is balanced by the drift of minority carriers back across the junction due to the built-in electrostatic field [18].

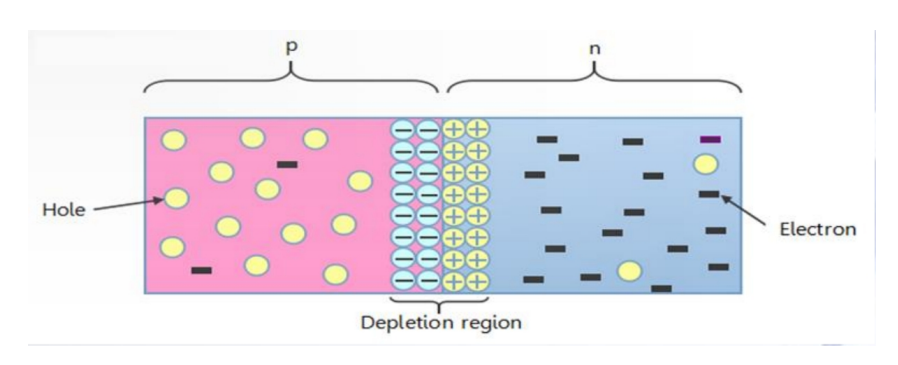


Figure 1.6: P-n junction at equilibrium [19].

1.4.3 Forward-biased p-n junction solar cell:

When the diode is connected to a forward-biased external voltage, the depletion region narrows. The negative charge carriers (electrons) and positive charge carriers (holes) are pushed away from the negative and positive terminals, respectively, toward the p-n junction. As a result, the energy required for the charge carriers to cross the depletion region is reduced. Once the applied voltage reaches the barrier potential, electrons begin to flow through the space charge region. The current through the diode increases exponentially as the forward bias voltage increases [14]. The current in forward bias mode is described by the ideal Shockley equation as follows [14]:

$$I_d = I_0(exp(\frac{e.V}{KT}) - 1) \tag{1.8}$$

1.4.4 Reverse-biased p-n junction solar cell:

If the P-region is linked to the negative terminal and the N-region to the positive terminal of the external power source, the PN junction will be in a reverse-biased condition. When the P-region is connected to the negative voltage, the holes in the P-region will be attracted to the external voltage and begin to move away from the depletion region. A similar effect occurs with the electrons. As a result, a small current, ranging from a few nanoamperes to microamperes, will flow. This current is known as the reverse saturation current [20].

1.4.5 P-N junction solar cell under illumination:

When a solar cell is exposed to light, the photons incident on the cell generate electron-hole pairs. Through diffusion within the material, these electrons and holes move towards the junction. At the junction, the built-in electric field separates the positive and negative charge carriers. The charge carriers are then extracted through electrical contacts, contributing to the output current in the external circuit. This process ultimately converts the chemical energy of the charge carriers into electrical energy. Once electrons have passed through the circuit, they recombine with holes at the metal-absorber interface.

After the electron-hole pairs are created through light absorption, they move within the crystal lattice. Before recombining, these charges must be collected in order to extract power from the photovoltaic (PV) cell. The generation of electrical currents in this process relies on the movement of the electron-hole pairs, making the Drift-Diffusion (D-D) model the appropriate mechanism to describe the behavior of charge carriers in the substrate under the influence of light and/or an electric field, causing a deviation from thermal equilibrium [21].

Therefore, the total current passing through the illuminated solar cell will be [22]:

$$I = I_0(exp(\frac{q.V}{\eta kT}) - 1) - I_{ph}$$
(1.9)

Where I_{ph} is photogenerated current.

1.4.6 Metal-semiconductor junction:

The type of metal-semiconductor junction depends on the work functions of the metal and semiconductor. When the metal's work function is lower than that of the semiconductor ($\Phi_m < \Phi_s$), a non-rectifying Ohmic junction is formed. Here, us represents the semiconductor's work function. The work function of a material is defined as the energy required to move an electron from the Fermi level to the vacuum level. On the other hand, if the metal's work function is higher than the semiconductor's ($\Phi_m > \Phi_s$), a rectifying Schottky junction is created. It depends also on the semiconductor type (n-type or p-type) [17,23].

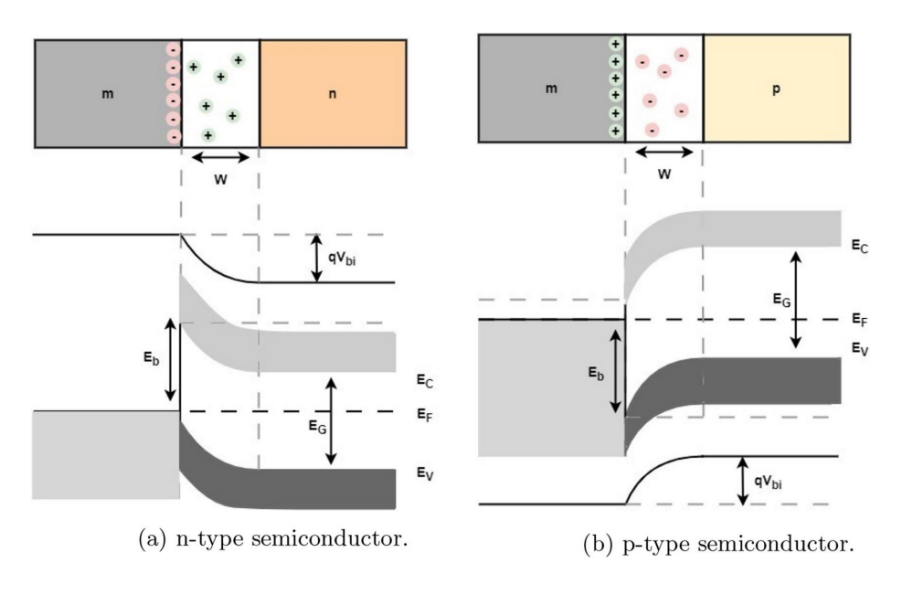


Figure 1.7: Band diagrams of metal-semiconductor junction [17].

1.5 Solar Cell I-V Characteristics:

The I–V characteristics of solar cells, serve as a crucial tool for evaluating their performance, it is also useful for analyzing and understanding the internal physical processes of the PV solar cell [24,25].

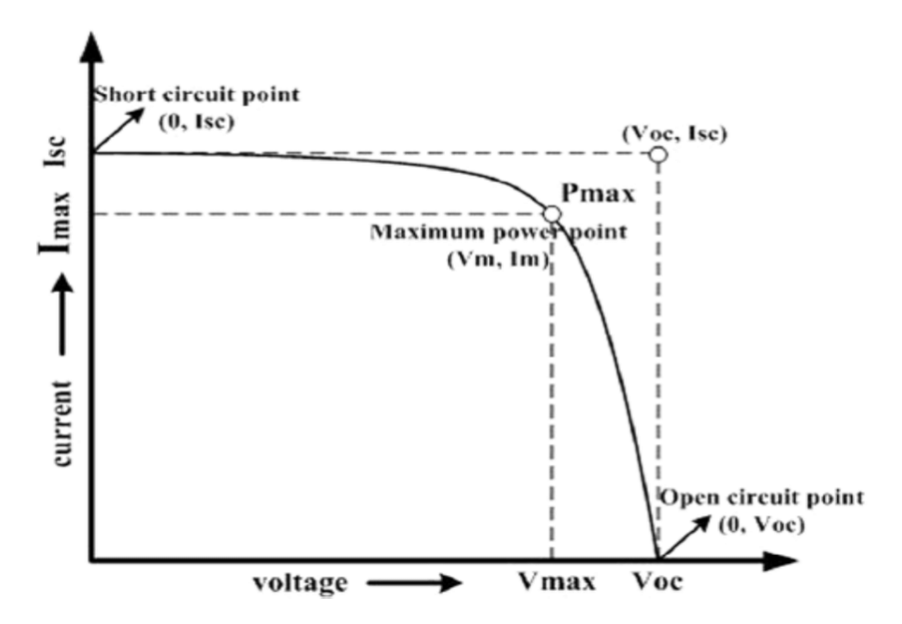


Figure 1.8: I-V characteristic curve of a solar cell [26].

1.5.1 Short-circuit current:

The short-circuit current represents the maximum current a solar cell produces when its electrodes are short circuited. This current is influenced by the solar irradiance spectrum and the area of the solar cell. To eliminate the effect of the cell's size, the short-circuit current density is commonly used to characterize the maximum current output of the solar cell [27].

1.5.2 Open-circuit voltage:

The open-circuit voltage of a solar cell is the maximum voltage that occurs when no current flows through the external circuit, meaning the cell is open-circuited. It represents the forward bias voltage at which the dark current balances the photocurrent. Denoted as V_{oc} , it is calculated under the assumption that the net current is zero [27], and can be expressed as follows [27]:

$$V_{oc} = \frac{KT}{q} \cdot \ln[\frac{I_{ph}}{I_0} + 1] \tag{1.10}$$

1.5.3 Efficiency:

The efficiency of a cell is defined as the ratio of the power it produces (the output power) to the power it receives (the input power). To determine the cell's efficiency for a specific load resistance, it is necessary to calculate the maximum power point. The output power is calculated by multiplying the current and voltage: P = IV. This power is typically displayed as a curve that shows the relationship between the out-

put voltage and the power produced. The figure also highlights the maximum power point (MPP), which represents the point where the solar cell generates its maximum power. The input power, which is not an electrical quantity, is determined using the irradiance. The irradiance G_{inc} , representing the radiant flux (power) received per unit area, is multiplied by the active area of the solar cell to calculate the total incident power [28], the efficiency expression is given by [28]:

$$\eta = \frac{P_{max}}{P_{inc}} = \frac{I_{max}.V_{max}}{G_{inc}.A_{active}} \tag{1.11}$$

1.5.4 Fill factor:

The fill factor (FF) is the ratio of the maximum generated power to the product of the open-circuit voltage and the short-circuit current. It provides an initial indication of the cell's quality. A perfect p-n junction would have an ideal I(V) curve shaped like a rectangle, resulting in a FF of 100%. However, FF can also be used to compare different types of solar cells [28]. The fill factor expression is given by [28]:

$$FF = \frac{P_{max}}{I_{SC}.V_{OC}} = \frac{I_{max}.V_{max}}{I_{SC}.V_{OC}}$$
 (1.12)

1.6 Photovoltaic cells development:

Photovoltaics have become a big part of the shift towards cleaner energy in the last ten years. This is thanks to improvements in solar cells manufacturing methods and the materials used. However, several challenges remain before photovoltaics can deliver cleaner and more affordable energy. Photovoltaic cells are classified into four main generations: first, second, third, and fourth [29].

1.6.1 First generation of photovoltaic cells:

Silicon-based photovoltaic cells were the first to enter the market, using materials and techniques from the microelectronics industry. They now account for over 80 % of global installed capacity and 90% of the market share, due to their high efficiency. The first generation includes mono-, poly-, and multicrystalline silicon, along with single III-V junctions like GaAs [29].

1.6.1.1 Monocrystalline silicon (m-Si)-based solar cells:

Monocrystalline silicon solar cells are made by growing silicon blocks from small monocrystalline seeds and then slicing them into wafers using the Czochralski process (Figure 1.10(a)). This material is favored for its high efficiency compared to multicrystalline

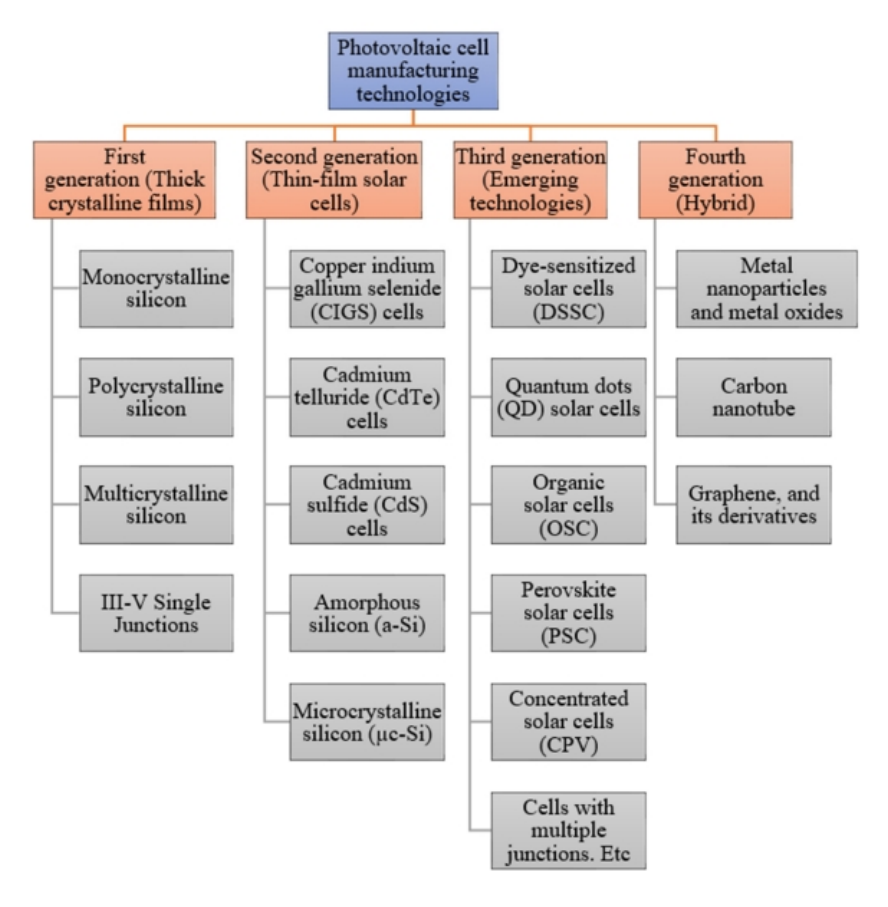


Figure 1.9: Development in photovoltaic cell technologies [29].

silicon. However, these cells face several challenges, including strict purity requirements, high material usage during cell production, complex manufacturing processes, and limitations in the size of modules made from these cells. Their efficiency is between 15% and 24% with 1.1 eV Band gap [29].

1.6.1.2 Polycrystalline silicon (p-si)-based solar cells:

Polycrystalline solar panels are produced differently from monocrystalline ones. Rather than cutting the panels, manufacturers melt the silicon and pour it into molds, which is a simpler and more cost-effective manufacturing process. Its efficiency ranges from 10% to 18%, with a band gap of approximately 1.7 eV and a lifespan of 14 years. The advantages of these cells include a simple and profitable manufacturing procedure, reduced silicon waste, and higher absorption compared to multicrystalline silicon. However, its restrictions include lower efficiency and higher sensitivity to temperature [29].

1.6.1.3 Multicrystalline silicon-based solar cells:

Multicrystalline silicon blocks are created by melting high-purity silicon and crystallizing it in a large crucible using the directional solidification process (Figure 1.10(b)). Unlike the Czochralski process, there is no reference crystal orientation, so the silicon

material produced has various orientations [29].

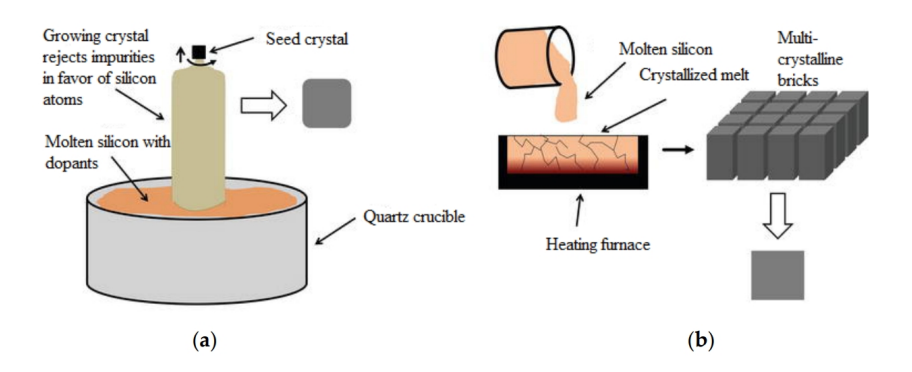


Figure 1.10: Schematic representation of: (a) the Czochralski process for producing monocrystalline blocks and (b) the directional solidification process for creating multicrystalline blocks [29].

1.6.1.4 Single III-V junction (GaAs)-based solar cells:

III-V materials offer the highest photovoltaic conversion efficiency, reaching 29.1% with a GaAs single junction under standard sunlight and 47.1% for a six-junction device under concentrated sunlight. These devices are also thinner, with absorption layers typically 2 to 5 μ m thick, making them suitable for lightweight, flexible applications on curved surfaces. Additionally, III-V devices are known for their high stability and have a proven track record of excellent performance in demanding applications, such as in space [29].

1.6.2 Second generation of photovoltaic cells:

Thin film photovoltaic cells, made from materials like CdTe, gallium selenide, CIGS, or amorphous silicon, offer a lower-cost alternative to crystalline silicon cells. They provide better mechanical properties for flexible applications but may have reduced efficiency. The evolution of thin films introduced new growth techniques and expanded the field into areas like electrochemistry [29].

1.6.2.1 Amorphous silicon-based photovoltaic cells:

Amorphous silicon (a-Si) solar cells are the most widely used thin film technology, with efficiencies ranging from 5% to 7%, and reaching 8–10% in double and triple junction structures. Variants of amorphous silicon include amorphous silicon carbide (a-SiC), amorphous germanium silicon (a-SiGe), microcrystalline silicon (μ -Si), and amorphous silicon nitride (a-SiN). Hydrogen is used to dope the material, resulting in hydrogenated amorphous silicon (a-Si:H) [29].

1.6.2.2 CdTe solar cells:

Cadmium telluride (CdTe) is a leading thin-film photovoltaic technology, with strong solar absorption and a direct bandgap of 1.45 eV. It has high efficiency, with record efficiencies of 21.0% for cells and 17.5% for modules. CdTe offers low module costs but requires high processing temperatures. Concerns about cadmium's toxicity and tellurium's scarcity have led to research into alternative materials that are easier to manufacture and rely on abundant, non-toxic elements [30].

1.6.2.3 CIGS solar cells:

Copper indium gallium diselenide (CIGS) is a compound semiconductor with a bandgap of 1.1-1.2 eV, holding 2% of the global PV market and 22% of the thin-film market in 2013. CIGS films can be applied to flexible substrates, making them suitable for unconventional PV applications, and they are highly resistant to radiation. Record efficiencies for CIGS are 21.7% for cells and 17.5% for modules. Key challenges include variability in film properties, low open-circuit voltage, and the limited availability of indium, which could affect large-scale deployment [30].

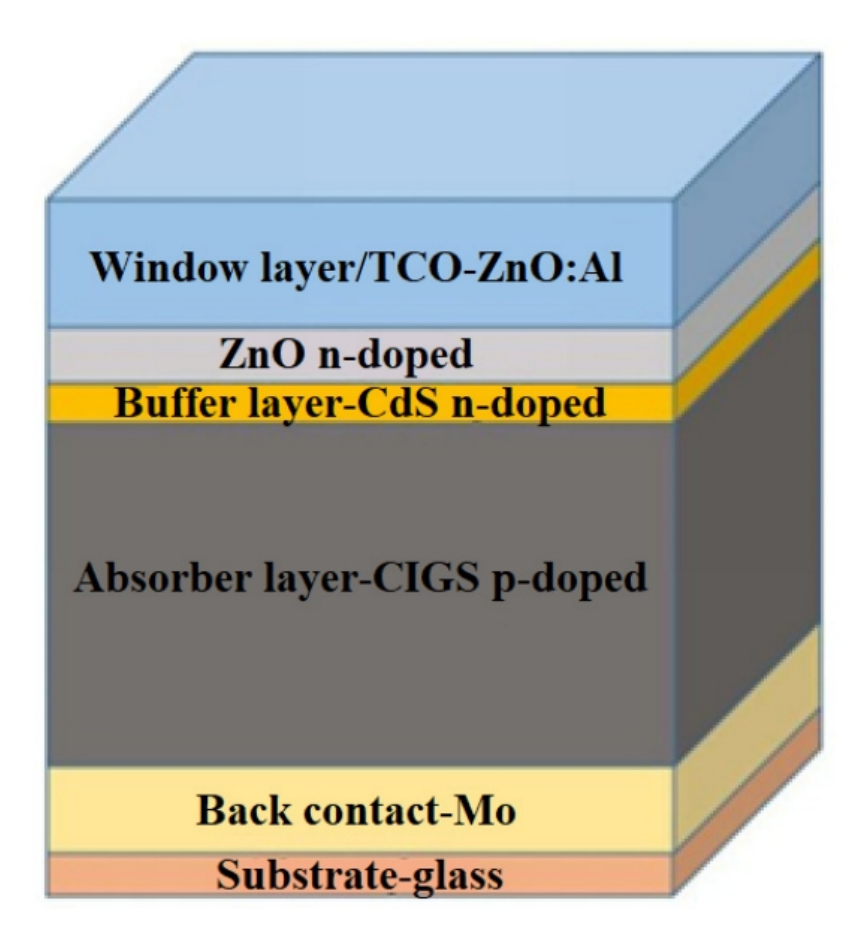


Figure 1.11: Demonstration of the CIGS-based solar cell [29].

1.6.2.4 Kesterite solar Cells:

Copper zinc tin sulfide (Cu₂ZnSnS₄, or CZTS) is an abundant Earth-based alternative to CIGS, sharing similar processing methods and challenges. One major issue is managing cation disorder, where the uncontrolled substitution of Cu and Zn cations creates point defects that can impede charge extraction and lower open-circuit voltage. The highest certified cell efficiency for CZTS has reached 12.6% [30].

1.6.3 Third generation of photovoltaic cells:

The third generation of solar cells includes various technologies, from low-cost, low-efficiency systems (like dye-sensitized and organic cells) to high-cost, high-efficiency systems (like III-V multi-junction cells). These technologies are used in applications ranging from building integration to space. Despite some being studied for over 25 years, they are often called "emerging concepts" due to their limited market adoption [29].

1.6.3.1 Organic and polymeric materials photovoltaic cells (OSC):

Organic photovoltaics (OPV) utilize organic small molecules or polymers to absorb light. These materials primarily consist of elements that are abundant on Earth and can be fabricated into thin films using large-area, high-throughput deposition techniques. Organic multijunction cells are potentially easier to manufacture than traditional III-V multi-junctions due to their high defect tolerance and simpler deposition process. Small-molecule and polymer OPV cells have achieved certified efficiencies of 11.1%, with module efficiencies reaching 8.7%. However, challenges remain, including inefficient exciton transport, poor long-term stability, low large-area deposition yield, and limited maximum efficiency [30].

1.6.3.2 Dye-sensitized photovoltaic cells (DSSC):

Dye-sensitized solar cells (DSSCs) are a mature nanomaterial-based technology featuring a nanoporous TiO2 anode sensitized with dye molecules. They use a liquid electrolyte for ion transport, though solid-state versions have also been developed. DSSCs can achieve efficiencies up to 12.3%, with benefits like low-cost materials, simple assembly, and flexible modules. However, challenges include limited long-term stability under light and high temperatures, low near-infrared absorption, and low open-circuit voltages due to interfacial recombination [30].

1.6.3.3 Perovskite solar cells:

Perovskite solar cells (PSCs) represent a groundbreaking photovoltaic technology that utilizes metal halide perovskites (MHPs), such as methylammonium iodide and formamidinium lead iodide (MAPbI3 and FAPbI3, respectively). MHPs offer several advantages for photovoltaic absorbers, including a direct band gap with a high absorption coefficient, long carrier lifetime and diffusion length, low defect density, and the ability to easily adjust their composition and band gap [29].

1.6.3.4 Quantum dots photovoltaic cells:

Solar cells made from these materials are referred to as quantum dots (QDs), or nanocrystalline solar cells. They are created through epitaxial growth on a substrate crystal. Quantum dots are encased by high potential barriers in a three-dimensional structure, causing the electrons and electron holes within them to have discrete energy levels due to confinement in a small space (Figure 14). As a result, the ground state energy of the electrons and electron holes in a quantum dot is dependent on the size of the quantum dot [29].

1.6.3.5 Multi-junction photovoltaic cells:

Multi-junction (MJ) solar cells are composed of multiple p-n junctions made from different semiconductor materials, with each junction generating electric current in response to light of a specific wavelength. This design enhances the conversion of incident sunlight into electricity, improving the cell's efficiency. The idea of using materials with varying band gaps to capture the maximum number of photons is known as a tandem solar cell. A single cell can be made from the same or different materials, offering a wide range of design possibilities [29].

1.6.4 Forth generation of photovoltaic cells:

Fourth-generation photovoltaic solar cells integrate the advantages of earlier generations, including lower costs, flexibility, and the high stability of third-generation materials such as nanomaterials, metal oxides, graphene, and carbon nanotubes. These features will lead to improved solar cell devices that offer cost-effective manufacturing, enhanced durability, and efficient performance. The use of nanomaterials in solar devices will help increase charge dissociation and transport within the cells. Due to its remarkable properties and allotropic forms that span all four dimensions, graphene holds significant promise as a potential material for solar cells in fourth-generation technological advancements [31].

1.6.4.1 Graphene-Based Photovoltaic Cells:

The fourth generation of solar cells offers exceptional affordability and flexibility by utilizing thin polymer layers, metal nanoparticles, various metal oxides, carbon nanotubes, graphene, and their derivatives. Special attention has been given to graphene, as it is regarded as a nanomaterial of the future. Due to its unique properties, including high carrier mobility, low resistivity, high transmittance, and 2D lattice structure, graphene-based materials are being explored as potential alternatives to traditional materials in photovoltaic devices. Graphene-based solar cells work like traditional inorganic cells, but with graphene replacing inorganic materials. Graphene improves adaptability and tunability, with efficiency largely determined by the number of graphene layers and doping effects [29,31].

Chapter 2

Overview of the Materials Used

Over the past 50 years, numerous efforts have been made to obtain graphene sheets. The goal has been to explore the properties of a single-atom-thick, densely packed layer composed of sp2 carbon. Previous attempts yielded limited success, and the primary focus of research until the 1990s was the intercalation of graphitic compounds. Finally, in 2004, Andre Geim's team achieved success by isolating individual graphite layers at Manchester University. The individual graphite layers extracted from bulk graphite after isolation were referred to as graphene [32].

The discovery of graphene and its remarkable physicochemical properties and applications paved the way for the exploration of a wide range of two-dimensional (2D) materials, which have attracted significant research interest in recent years due to their exceptional characteristics [33]. Transition metal dichalcogenides (TMDs) are a class of two-dimensional materials known for their diverse optoelectronic characteristics. Among them, molybdenum disulfide (MoS_2) is the most extensively researched for nanoelectronics applications due to its semiconducting nature [34].

On the other hand, indium phosphide (InP) is a direct bandgap semiconductor known for its high light absorption capability and efficient charge transport, making it a strong candidate for high-performance solar cell applications.

This chapter provides a comprehensive overview of MoS_2 and InP, the two materials used in the solar cell investigated in this study, focusing on their crystal structures and their optical and electronic properties.

2.1 Materials at the nanoscale

Nanomaterials are a branch of material science focused on studying materials that have at least one dimension at the nanometer scale. At this scale, significant changes in the physicochemical properties and reactivity of materials are linked to the number of atoms or molecules that make up the material. For example, size-dependent properties such as surface plasmon resonance in metal nanoparticles, quantum confinement in

semiconductor particles, and superparamagnetism in magnetic nanomaterials can be observed. When only one dimension is confined, the material typically takes a layered or 2D form; if two dimensions are restricted, the material becomes a 1D, wire-like structure; and when all dimensions are within the nanometer range, the material is often referred to as a 0D material. Among these, 2D nanomaterials stand out as the most exciting class, offering promising properties and potential [17,35].

2.2 Two-dimensional materials

2D nanomaterials, with their high aspect ratio, exhibit remarkable properties that are notably distinct from those of bulk materials. Additionally, they possess excellent charge carrier mobility, making them highly suitable for solar device applications. Their flexibility is also a key advantage in the design of flexible electronics and sensors. Furthermore, these materials showcase unique optical properties, such as plasmonic effects, light sensitivity, and enhanced emission and absorption characteristics [17]. Graphene, a single layer of graphite just one atom thick, was one of the first true twodimensional materials to be isolated in nature. Over the past fifty years, considerable effort has been devoted to obtaining single layers of graphite (graphene sheets) in order to unlock the predicted properties of a tightly bonded, one-atom-thick layer of sp2 carbon. In reality, many techniques have been explored over this time, but only with limited success [35]. Over this period, research has expanded beyond graphene to include other 2D materials, such as transition metal dichalcogenides (TMDs like WS2, MoS_2), topological insulators (TIs such as MnBi2Te4), and newly discovered 2D non-noble metals (like 2D Ga and 2D In). These materials have attracted significant attention due to their tunable bandgaps, surface and edge reactivity, unique electronic and optoelectronic properties, and the development of multilayer architectures with atomically sharp interfaces [36].

2.3 Molybdenum disulfide

Molybdenum disulfide (MoS_2) is an inorganic compound belonging to the transition metal dichalcogenide (TMD) family. It is one of the most widely used photocatalysts, with applications spanning various fields. Recently, MoS_2 has gained significant attention due to its unique electrical and optical properties. MoS_2 is a two-dimensional (2D) TMD, a semiconductor with a narrow band gap of 1.9 eV, which can be modified by adjusting the number of layers. Among all 2D TMDs, MoS_2 is one of the few with a natural layered structure, allowing for the easy extraction of high-quality 2D MoS_2 without the need for complex chemical synthesis. As a result, the cost of producing 2D MoS_2 is significantly lower compared to other 2D TMDs due to simpler preparation

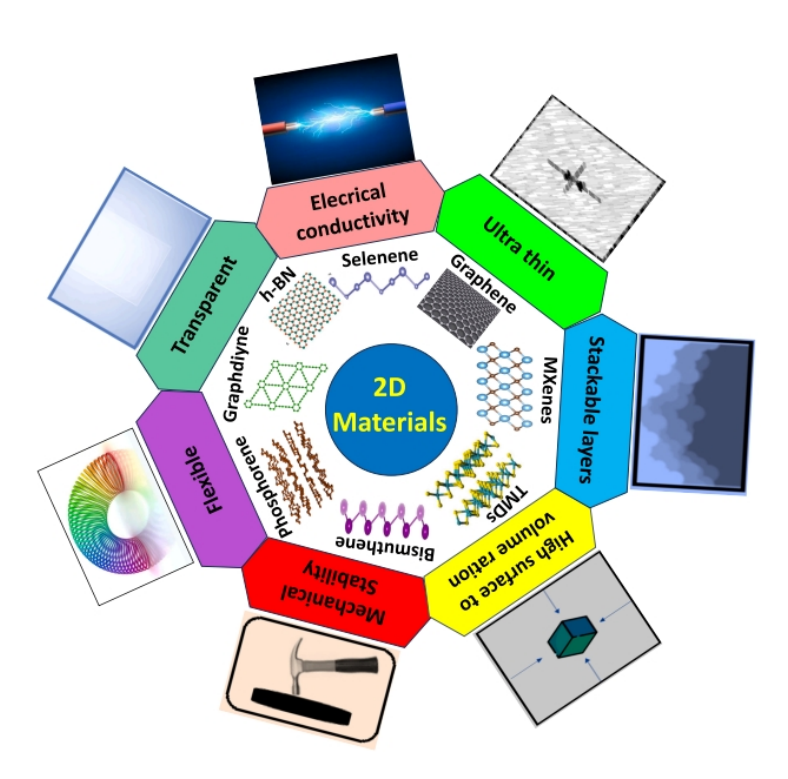


Figure 2.1: Schematic depiction of 2D materials and their properties [37].

methods. Furthermore, 2D MoS_2 is a direct band-gap semiconductor, offering superior electrical performance compared to other 2D TMDs. These characteristics make MoS_2 particularly appealing in the realm of 2D materials [5].

2.3.1 Cristal structure

Molybdenum disulfide (MoS_2) is a black solid with a bright color and is the primary ore of molybdenum. The crystal phases of bulk MoS_2 can take various forms depending on how the Mo atoms are coordinated, such as 1T MoS_2 , 2H MoS_2 , and 3R MoS_2 . The structures of these three polymorphs are shown in Figure 2.2. In these polymorphs, the first number indicates the number of monolayers in the unit cell, while the last three letters—T, H, and R—represent trigonal, hexagonal, and rhombohedral symmetries, respectively. Each phase has distinct characteristics that arise from variations in the symmetry of the layers [37]. 1T- MoS_2 is the most thermodynamically stable polymorph of MoS_2 at elevated temperatures. The Mo atoms are arranged in a trigonal prismatic coordination, with a distorted octahedron formed by the six nearest sulfur atoms. Its crystal structure is defined by the presence of a single type of sulfur atom in the lattice, exhibiting metallic properties. $2H-MoS_2$ is the most prevalent form of MoS_2 found in nature. It features a hexagonal crystal structure, with each Mo atom surrounded by six sulfur atoms arranged in a trigonal prism. Its unit cell contains two distinct sulfur sites within the lattice, and demonstrates semiconductor properties [38, 39], the adjacent layers are stacked in an ABA pattern, with the middle layer

slightly offset from the top and bottom layers. This configuration enables strong interlayer interactions between sulfur atoms, leading to a stable crystal structure, where sulfur atoms from different planes align in the same positions relative to one another. The $3R-MoS_2$ polymorph exhibits a rhombohedral crystal structure and is typically observed at low temperatures. Its lattice parameter falls between those of the 1T and 2H structures, and it features three distinct sulfur sites within the lattice [39].

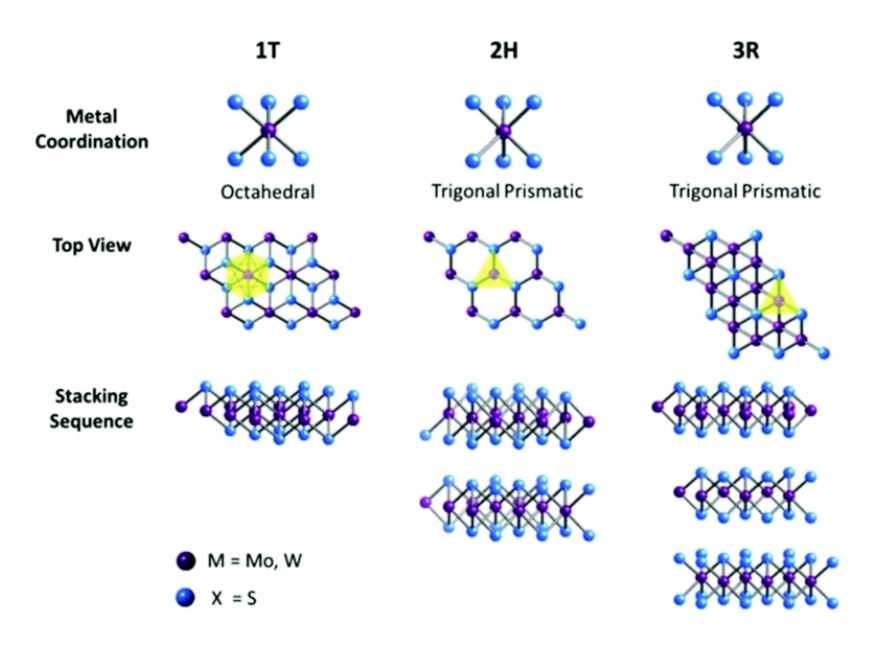


Figure 2.2: Various coordination and stacking arrangements of the three MoS_2 structures: 1T, 2H, and 3R [40].

A single layer of MoS_2 has an S-Mo-S structure, resembling a sandwich (see figure 2.3). Typically, each layer is about 0.65 nm thick [41]. The atoms are bonded together by covalent bonds, while the layers are held together by weak van der Waals forces [42], these weak forces arise from temporary dipole moments caused by slight displacements in the electron cloud around the atoms [39]. The Mo-S bond length, crystal lattice constant, and the distance between the sulfur atoms on the upper and lower sides measure 2.4, 3.2, and 3.1 Å, respectively. It is found that monolayer MoS_2 exists in two phases: metallic 1T and semiconducting 2H . MoS_2 can act as a semiconductor with direct band gap of 1.96 eV. This suggests that the material has strong absorption in the visible region of the solar spectrum, making it suitable for use as a co-catalyst [42]. For example, monolayer MoS_2 differs from its bulk form in that it has a direct band gap, making it potentially useful for applications in piezoelectric electronics and optoelectronics. Therefore, surface modifications, such as the addition of atoms and defects that induce surface ferroelectricity and piezoelectricity, can significantly alter the piezoelectric properties of 2D materials. Most studies on electronics and energy-related reactions focus on the 2H and 1T phases of MoS_2 [37].

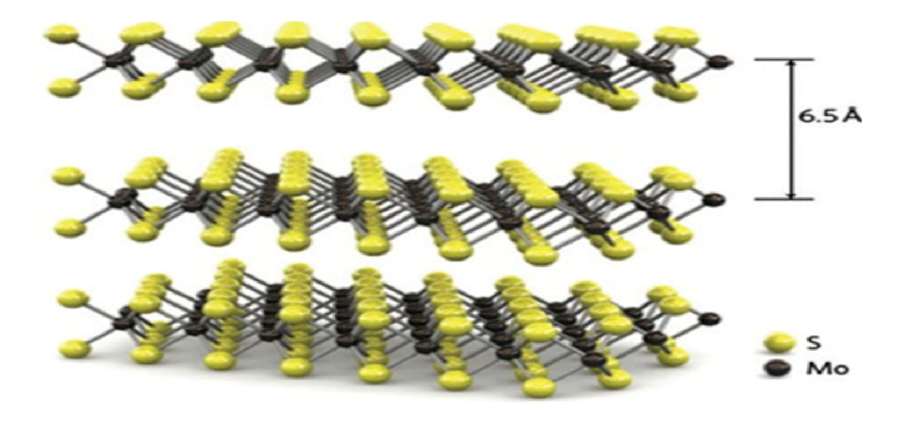


Figure 2.3: The crystal structure of MoS_2 [43].

2.3.2 Properties

The properties of MoS_2 are essential in determining its effectiveness for energy storage applications. It boasts remarkable features such as high electrochemical activity, rapid ion diffusion, and excellent electrical conductivity, making it a highly preferred material for electrodes in batteries and supercapacitors. These characteristics significantly influence its performance in energy storage, largely due to its large surface area, which provides a substantial active site for electrochemical reactions [39].

2.3.2.1 Optical propeties

The absorption coefficient and refractive index are key parameters that define how a material responds when a specific wavelength passes through it. The absorption coefficient indicates the distance a light wave travels within a material before being absorbed [40]. When the energy of incident photons is smaller than the material's bandgap energy, the material appears transparent to that light. The absorption coefficient determines how deep light of a specific wavelength can penetrate into a material before being completely absorbed. Due to a phenomenon called fundamental absorption, the absorption coefficient increases rapidly for light with wavelengths shorter than the bandgap [44]. Figure 2.4 shows that monolayer MoS_2 exhibits relatively high absorption coefficient in the visible spectrum near 400nm. The curve also display a sharp decline in the absorption coefficient after 500nm, indicating that a MoS_2 -based photodetector is effective only in detecting light below 500nm.

The refractive index of a material is the ratio of the speed of light in a vacuum to the speed of light within that material [44]. Figure 2.5 illustrates how the refractive index of monolayer MoS_2 changes with wavelength. Below 400nm, it is observed that the refractive index ranges between 1 and 3, followed by a sudden increase above 400nm. Then the curve shows a gradual decline at higher wavelengths.

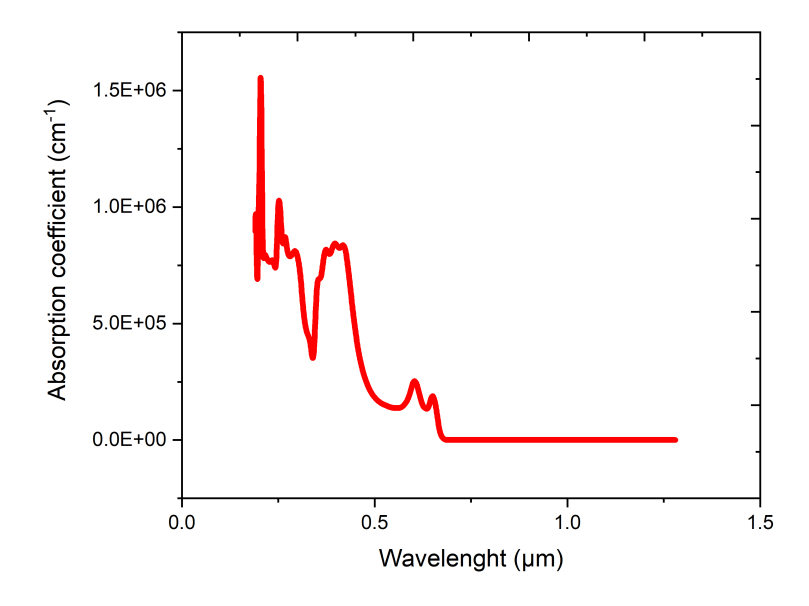


Figure 2.4: The absorption coefficient of mono-layer MoS_2 [45].

One of the key advantages of MoS_2 in optoelectronics is its tunable bandgap, which changes based on size and structure. Different bandgaps enable tunable photoresponsivity (R), specific detectivity, and response time, making MoS_2 suitable for a broad range of applications [40].

2.3.2.2 Electronic properties

In this section, we will explore the density of states and band structure of MoS_2 . Multilayer MoS_2 has an indirect band gap of 1.2 eV, which increases as the number of layers decreases, reaching a direct band gap of 1.8 eV in monolayer MoS_2 . While the band gap of MoS_2 is relatively good, it still falls short of the 1.12 eV direct band gap found in silicon. The mechanical strain in MoS_2 can alter its band gap, transitioning it from a direct to an indirect band gap and turning the material from a semiconductor into a metal. The properties of MoS_2 are largely determined by the 4d orbitals of molybdenum (Mo) and the 3p orbitals of sulfur (S). The projected density of states (PDOS) for bulk and monolayer MoS_2 are quite similar, though there are some additional peaks in the PDOS for the monolayer form [40] as shown in figure 2.6. In general, transistors based on MoS_2 exhibit n-type behavior [41]. Doping monolayer MoS_2 with elements like chromium, copper, and scandium makes it an n-type semiconductor, while doping with nickel or zinc turns it into a p-type. Titanium (Ti) doping can result in either p-type or n-type behavior, depending on the doping concentration and site. At doping levels below 2.04%, MoS_2 behaves as p-type, but at 3.57% Ti interstitial doping, it becomes n-type due to an increase in surface dipole moment and a reduction in electron affinity. At high doping levels (7.69%), the Fermi level shifts into the con-

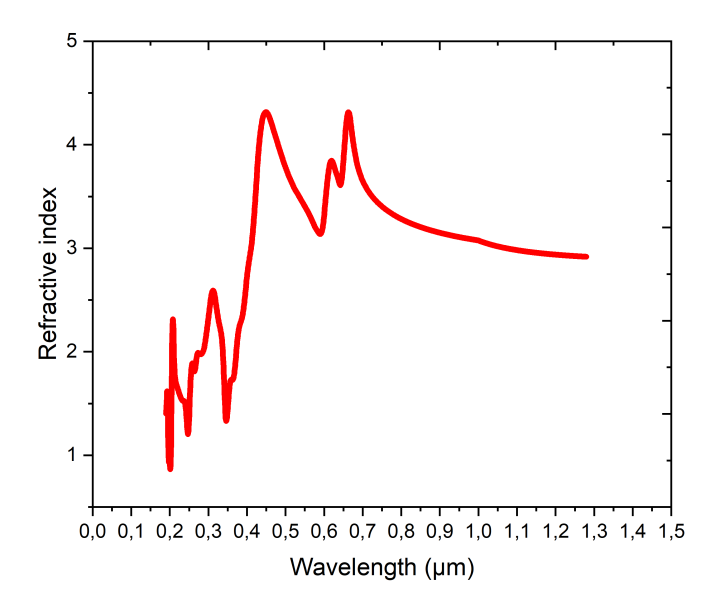


Figure 2.5: The refractive index of mono-layer MoS_2 [45].

duction band, converting MoS_2 into a ferromagnetic half-metal with complete spin polarization, which has potential for spintronic applications. However, substitutional Ti doping at any of the three concentrations did not significantly affect the electronic properties [40].

2.3.3 MoS_2 synthesis

Choosing an appropriate fabrication technique is essential to improve the desired properties of the synthesized MoS_2 . The weak van der Waals forces between MoS_2 layers have actually given rise to several synthesis techniques, each producing products with varying quantities, shapes, and sizes. These methods can be grouped into two categories: the top-down approach, where a sample's properties transition from a larger scale to a nanometric scale, and the bottom-up approach, which constructs MoS_2 nanosheets by assembling individual atoms [43,47].

2.3.3.1 Top-down approach

Mechanical exfoliation: The mechanical exfoliation technique involves extracting suitable MoS_2 flakes from the bulk crystal using adhesive tape and transferring them onto a specific substrate. Since no chemical reactions occur during the mechanical exfoliation process, the structure of MoS_2 remains unchanged. This method produces single-or few-layer MoS_2 nanosheets in various shapes and sizes once the tape is removed, leaving some MoS_2 residue on the substrate. These nanosheets are of high quality, making them ideal for studying the properties of the original material and for device

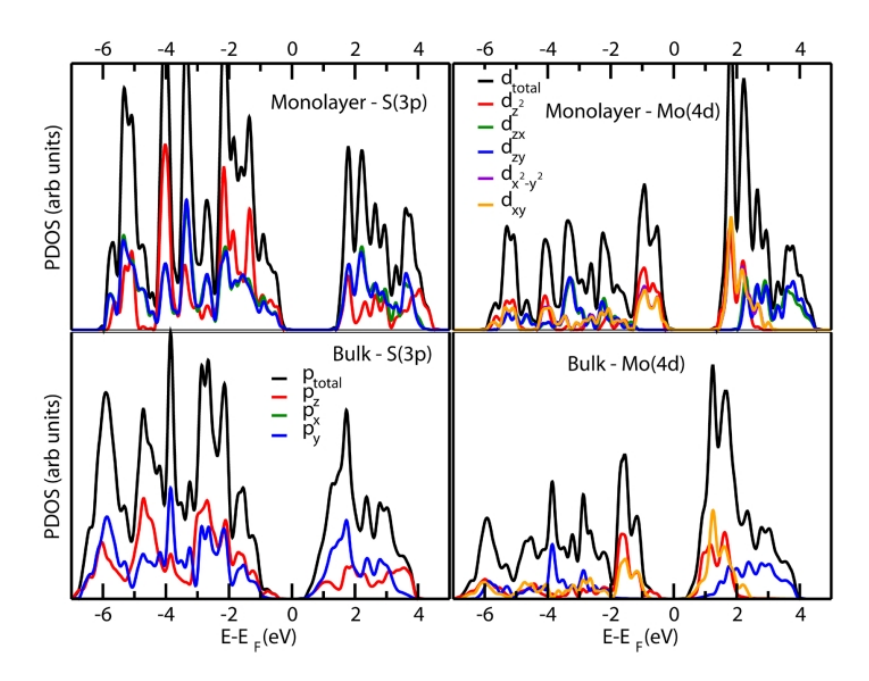


Figure 2.6: The calculated projected density of states (PDOS) for both bulk and monolayer MoS_2 are presented for Mo(4d) and S(3p) states. The legends for the p- and d-orbitals are the same for both the monolayer and bulk forms [46].

performance testing. However, the production yield is relatively low, and controlling the particle size of the resulting MoS_2 nanosheets is challenging [39].

While mechanical exfoliation using adhesive tape was the first successful technique for isolating 2D materials, ball milling employs a similar method but is better suited for large-scale production. Initially, ball milling was used to break and mix metallic powders to create alloys. Today, it is applied to the large-scale exfoliation of 2D materials in layers. As the balls roll and rebound in the mill with the 2D material, they exert shear, rolling, and impact forces, breaking van der Waals bonds and separating the 2D layers. This technique is generally divided into two categories: dry ball milling and wet ball milling. The latter technique requires the use of a special and costly organic solvent, which can lead to pollution and high expenses. On the other hand, dry ball milling is more aggressive and can induce defects in both the basal plane and the edges of the layered materials. These defects, however, can be beneficial for modifying the properties of 2D materials in applications like energy storage. They provide additional active adsorption sites, promote faster diffusion, and enhance storage capacity. It is crucial to determine the milling parameters to ensure both the quality and yield of the product [43].

Liquid phase exfoliation: Liquid phase exfoliation (LPE) of molybdenum disulfide (MoS_2) involves dissolving MoS_2 crystals in a solvent or solution, followed by exfoliating them into thin layers using mechanical, chemical, or thermal methods. This approach is popular due to its simplicity, cost-effectiveness, and efficiency in producing MoS_2 sheets with exceptional properties. LPE offers additional advantages, including

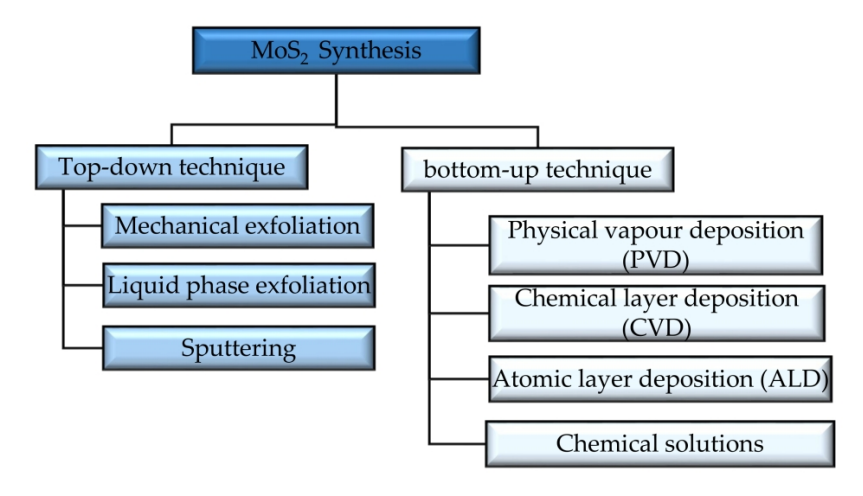


Figure 2.7: Various methods for synthesizing MoS_2 [47].

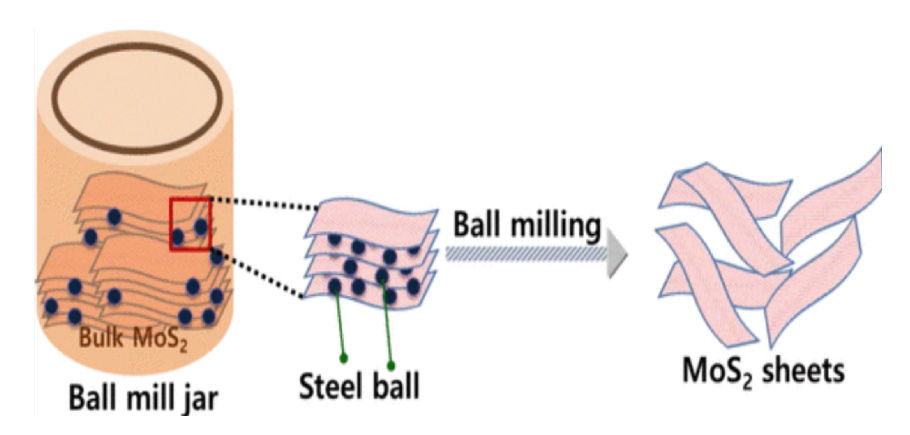


Figure 2.8: Schematic representation of the mechanical milling process for producing MoS_2 sheets [48].

the ability to control the thickness of the exfoliated flakes, ease of chemical modification of flake surfaces, and compatibility with various support materials. These features make it widely used in applications such as electronic devices, sensors, and catalysts. To achieve MoS_2 exfoliation, several solvents are employed, including water, alkaline solutions (e.g., sodium carbonate Na_2CO_3 or potassium hydroxide KOH), and organic solvents (e.g., N-methylpyrrolidone (NMP), dimethylformamide (DMF), acetone, and chloroform). Using water as a solvent for exfoliation offers particular advantages. A recent study showed that water can serve as an alternative to organic solvents for dispersing MoS_2 nanosheets. While water dispersions are less stable than those in organic solvents, the resulting nanosheets can have lateral dimensions ranging from 500 nm to 50000 nm and are stabilized by electric charges [43].

Sputtering: Sputtering is an effective method for synthesizing MoS_2 thin films with low coefficients of friction. The sputtering conditions and parameters significantly impact the compositional and morphological characteristics of the films. Vacuum and magnetron sputtering are two commonly used techniques in research. The closed-field magnetron sputtering method can be used to apply solid lubricants to tools like

end mills, drills, and cemented-carbide inserts. In 1986, Bichsel, Buffat, and Lévy produced MoS_2 films using a planar magnetron system with radio-frequency (RF) sputtering and thoroughly studied how sputtering parameters, particularly substrate temperature control, affected the morphological properties of the films. In a 2008 study, Audronis et al. described coatings created through pulsed magnetron sputtering of loosely packed powder targets made from chromium and boron alloys containing 12.8%, 18.9%, and 24.0% MoS_2 . Additionally, a simple dip-coating technique was used to produce MoS_2 thin films [37].

2.3.3.2 Bottom-Up approach

Physical vapour deposition (PVD): Physical vapor deposition (PVD) is a bottom-up technique that includes processes like ion implantation and molecular beam epitaxy (MBE). This method is primarily used for thin layers of MoS_2 , and the resulting grain sizes can vary [40]. A thin film can be formed through the condensation of solid material, where the vaporized material condenses and nucleates on the substrate's surface to create a stable and solid film. Among the various physical vapor deposition (PVD) methods, thermal evaporation is the most commonly used technique by researchers. Wu et al. successfully synthesized a high-optical-quality monolayer of MoS_2 on insulating substrates such as SiO2, glass, and sapphire, achieving excellent optical quality and high crystallinity. Later, in 2015, Zhang and colleagues developed amorphous MoS_2 nanosheets with enhanced catalytic activity for the Hydrogen Evolution Reaction (HER) in acidic solutions. This improvement was attributed to their three-dimensional nanostructure, unstructured nature, and the availability of uncovered edge sites [37].

Chemical vapor deposition (CVD): CVD has become one of the most effective techniques for fabricating transition metal dichalcogenides (TMDs) with high crystal quality, tunable size and thickness, and excellent electronic properties. In a typical CVD process, solid precursors are heated to high temperatures, forming a film on a substrate, typically Si/SiO2 wafers. MoO3 powder, sulfur powder, vaporized sulfur, or H2S are commonly used as the precursors for Mo and sulfur. However, it has been found that using MoCl5 as the solid precursor on various substrates produces MoS_2 with a high surface area, increased density of active sites, and reduced electrical contact loss between the substrate and MoS_2 . The usual heating temperature for CVD ranges from 700 to 1000 °C, though it can be lowered to 150 to 300 °C under plasma-enhanced conditions. As sulfur vaporizes, it reacts with MoO3, resulting in the formation of MoO3-x. The nitrogen carrier gas then transports MoO3-x, which reacts with sulfur to form MoS_2 molecules (see figure 2.10) [47].

The atomic layer deposition (ALD): The atomic layer deposition (ALD) technique is recognized for producing high-quality thin films, even at low temperatures, typically

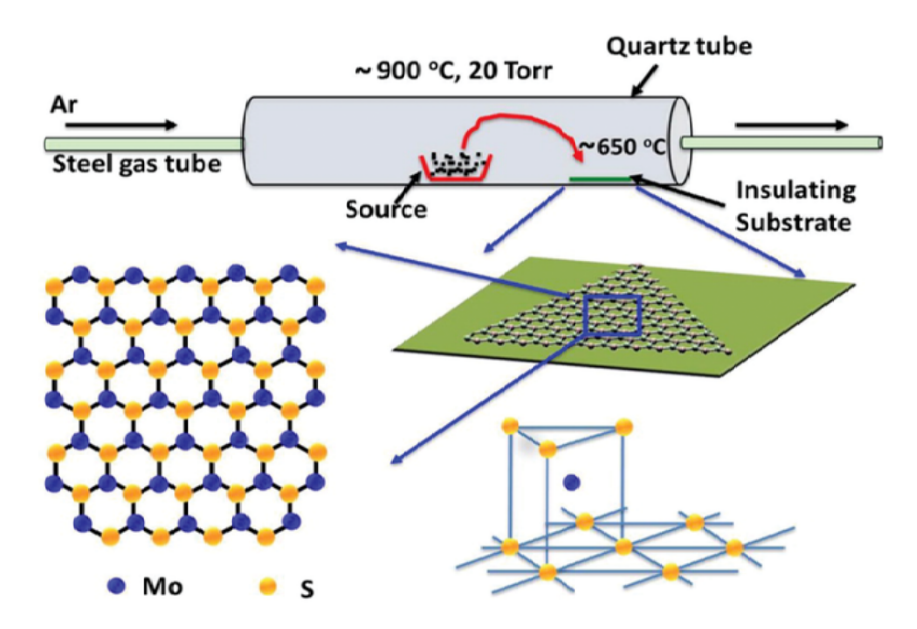


Figure 2.9: The process of synthesizing a 2D MoS_2 film on conventional insulating substrates using the PVD method [49].

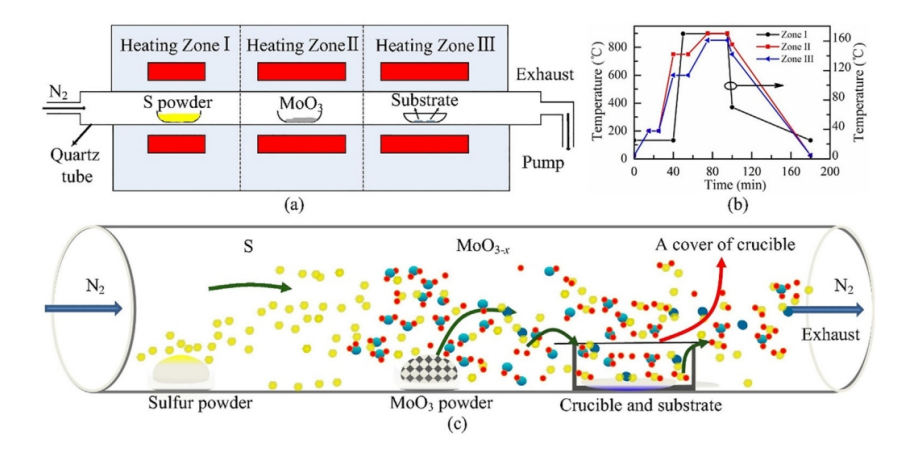


Figure 2.10: (a) A diagram depicting the three-zone CVD growth chamber.(b) The temperature program applied during the synthesis of monolayer MoS_2 .(c) A schematic showing the MoS_2 growth on a sapphire substrate [47].

ranging from 150 to 350 °C. ALD is a stepwise atomic growth process in which reactants are alternately introduced into the growth area, allowing for the purging of excess species and by-products after each reaction. This results in high-quality films through sequential surface reactions.

Despite the challenges associated with its synthesis conditions, ALD enables the deposition of crystalline MoS_2 thin films at relatively low temperatures (<350 °C), followed by annealing. For example, L.K. Tan et al. demonstrated the use of ALD for synthesizing highly crystalline MoS_2 films on sapphire substrates at 300 °C. They achieved this by alternately exposing the substrate to Mo(V) chlorides (MoCl₅) and hydrogen disulfide (H₂S) vapors. One key advantage of this process is the ability to deposit layered MoS_2 films on various substrates. ALD is a promising technique for producing

high-quality MoS_2 ultrathin films at low temperatures, offering excellent step coverage on various substrates. However, its very low throughput may limit its scalability and make it less competitive compared to other deposition methods [50].

2.3.4 MoS_2 in photovoltaic applications

 $2D\text{-}MoS_2$ displays remarkable optoelectronic properties, including a direct bandgap between 1.2 and 1.9 eV. These critical characteristics make MoS_2 highly promising for photovoltaic (PV) applications [50].In fact, studies have demonstrated that when a monolayer of n-type MoS_2 is deposited onto a p-type silicon substrate, the resulting p-n junction-based PV device can achieve a power conversion efficiency (PCE) of up to 5.23%.This achievement marks a major advancement in the use of monolayer TMDs for solar cell applications [39,50].

Perovskite solar cells (PSCs) were fabricated using a device structure of glass/FTO/ MoS_2 /perovskite-PO/spiro-OMeTAD/Au. As shown in Figure 2.11, these cells achieved a power conversion efficiency of 13.1%, comparable to PSCs employing conventional solid-state electron transport layers such as TiO_2 and SnO_2 [39].

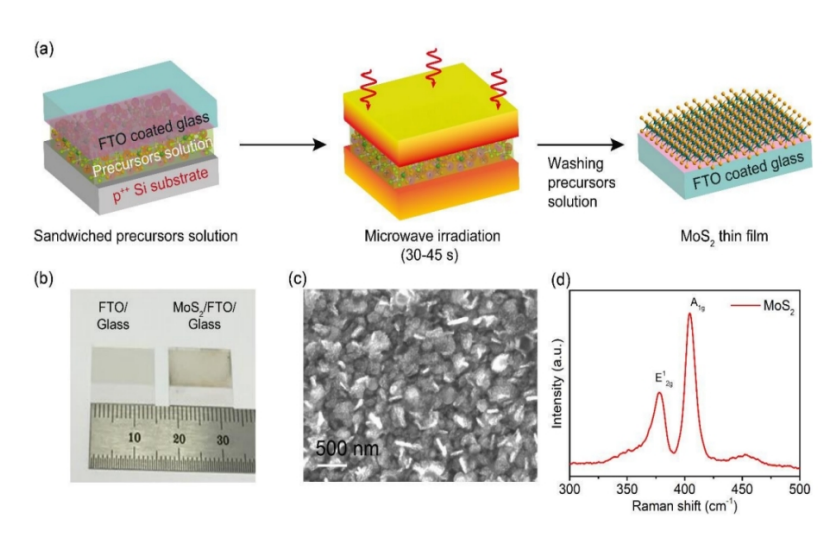


Figure 2.11: (a) Schematic illustration of the MoS_2 thin film synthesis on a glass/FTO substrate using the microwave-assisted method, (b) Camera image showing the MoS_2 thin film on the glass/FTO substrate alongside a bare glass/FTO substrate, (c) High-resolution FESEM image of the synthesized thin MoS_2 film, (d) Raman spectrum of the MoS_2 thin film showing the E1 2g and A1g vibrational modes peaks [39].

The MoS_2 /GaAs heterostructure positioned on hexagonal boron nitride has the capability to raise the power conversion efficiency (PCE) up to 9.03% [51].

 MoS_2 flakes have been employed as a buffer layer in copper zinc tin sulfide (CZTS) solar cells, achieving a notable efficiency of 17.03% along with improved thermal stability under elevated temperatures [52]. Additionally, MoS_2 can function effectively as either an electron transport layer (ETL) or a hole transport layer (HTL) [53]. a MoS_2 film was

employed in [54] to reduce defects and extend the depletion region in solar cells. This led to improved cell performance by lowering impurity concentrations and enhancing the built-in potential at the MoS_2 /p-Si interface. Table 2.1 provides a summary of the role of MoS_2 in solar cells [54].

Table 2.1: Applications of MoS_2 in solar cells [54].

Structure	Role of MoS_2	Enhanced property	
Graphene- MoS_2	Enhance the	Enhance the light absorbance	
Wedge-shaped microcavity	cell performance	to above 90%	
(Hg0.33 Cd0.66 Te)	Enhance the	Shift the cell absorbance to	
and monolayer MoS_2	cell performance	visible light range	
Microdome texture	Enhance the	Decreases reflections and traps	
on MoS_2 thin film	cell performance	light for incident angles (0-50)	
MoS_2 /GaAs over	Enhance the	PCE increased to 9.03%	
boron nitride	cell performance	TCE fricteased to 9.0376	
MoS_2 spray coating	HTL	PCE = 3.9%	
over perovskite cells			
5 monolayer MoS_2		$Jsc = 16.24 \text{ mA } cm^{-2}$	
nanosheets onto indium	ETL	Voc = 0.56 V	
tin oxide ITO substrate	LIL	(fill-factor) $FF = 0.37$	
thi oxide 110 substrate		PCE = 3.36%	
$ZnO-MoS_2$ -CZTS		$Jsc = 29.42 \text{ mA } cm^{-2}$	
	Buffer	Voc = 1.01 V	
		FF = 0.574 Efficiency = $17.03%$	
Organometallic-halide perovskite solar cell		Jsc \approx 22 mA cm^{-2}	
	Buffer	$Voc \approx 0.96 \text{ V}$	
		$FF \approx 0.6 \text{ PCE} = 14.9\%$	

2.4 Indium Phosphide

Indium phosphide (InP) is a key compound semiconductor belonging to the III–V group that exists in two crystalline forms: wurtzite (WZ) and zinc blende (ZB), with direct band gaps. It stands out due to its exceptional properties and is used in high-efficiency photovoltaic cells, integrated circuits, and microwave devices...etc [55]. InP has a moderate band gap, and it offers the highest thermoelectric figure of merit among its class of compounds, along with high electron mobility. Its wide-ranging application potential extends to advanced technologies such as optoelectronics, spin-tronics, thermoelectronics, high-speed low-power electronics, and photocatalysis [56].

2.4.1 Cristal structure

Indium phosphide features a zinc blende crystal structure, which belongs to the cubic lattice family. In this arrangement, indium and phosphorus atoms are organized into repeating cube-shaped units, with each unit cell containing four indium atoms and four phosphorus atoms, as shown in Figure 2.12. This type of crystal structure is consistent across all materials classified under zinc blende and is also one of the most prevalent structures found in semiconductors. The structure is similar to that of most group III-V semiconductors [57]. The crystal lattice consists of two face-centered cubic (FCC) sublattices—one composed of indium atoms and the other of phosphorus atoms—which are offset relative to each other along the (111) crystallographic direction [58].

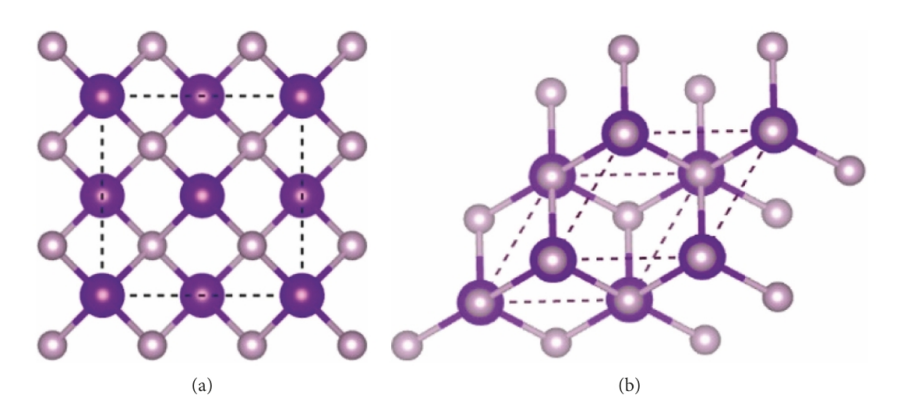


Figure 2.12: Unit cell crystal structure of indium phosphide shown in: (a) front view and (b) general view [59].

In recent years, it has also become feasible to grow InP in the metastable hexagonal Wurtzite (WZ) phase [60]. An ideal Wurtzite (WZ) structure is made up of two interpenetrating hexagonal close-packed (HCP) sublattices—one composed of atom type A and the other of atom type B—shifted relative to each other by $\frac{3}{16}$ c along the c-axis. These leads to two distinct stacking sequences: ABCABC··· along the (111) direction for the Zinc Blende (ZB) structure, and ABAB··· along the c-axis for the Wurtzite (WZ) structure [61] (see figure 2.13).

2.4.2 Electrical properties

InP has a direct band gap [62] of 1.344 ev [63] with its lowest energy point located at the Γ point. As illustrated in figure 2.14 The conduction band near its minimum in InP is parabolic and isotropic, meaning it has a single, well-defined electron effective mass. This mass is measured to be 0.082 at 77 K and 0.078 at 300 K. In contrast, the valence band is both degenerate and anisotropic, leading to a strong dependence of the effective masses of light and heavy holes on crystallographic direction. This directional dependence is especially significant for heavy holes, whose effective mass is greater along the (111) direction than along the (100) direction. The electron mobility in InP is primarily influenced by polar and acoustic phonon scattering at temperatures above 100 K. However, when the temperature drops below this threshold, piezoelectric and

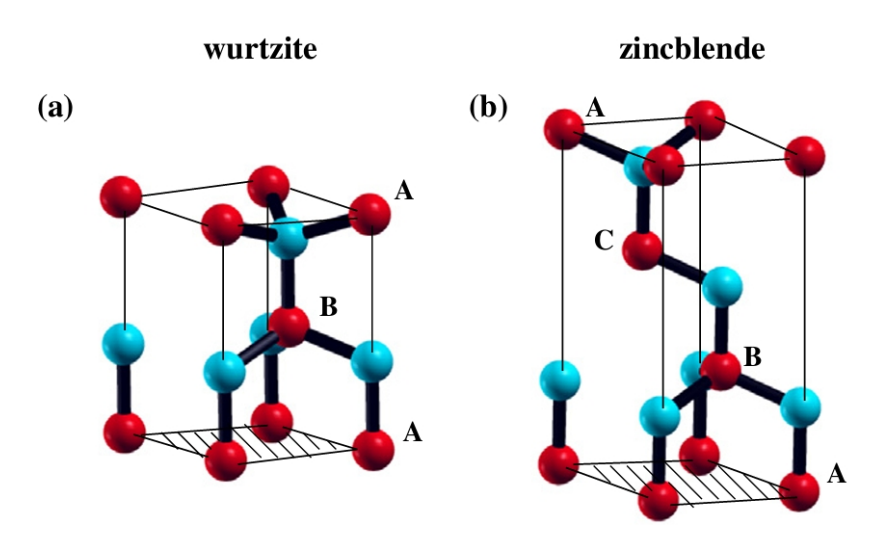


Figure 2.13: The two crystalline forms of InP: (a) Wurtzite (WZ) and (b) Zinc blende (ZB) [61].

impurity scattering become the dominant factors. In undoped bulk InP, typical electron mobility values are around 4000 to $5000 \ cm^2/V \cdot s$ at 300 K and between 30,000 to $50,000 cm^2/V \cdot s$ at 77 K. In doped samples, these mobility values are naturally reduced and vary depending on the dopant concentration and the level of compensation. n-type InP can be readily achieved by introducing group IV elements (which substitute indium atoms) or group VI elements (which replace phosphorus atoms). Among the commonly used dopants, tin and sulfur are favored by crystal manufacturers. P-type conductivity in InP is achieved by doping with shallow acceptor elements like cadmium, zinc, or beryllium, which replace indium atoms in the lattice [58].

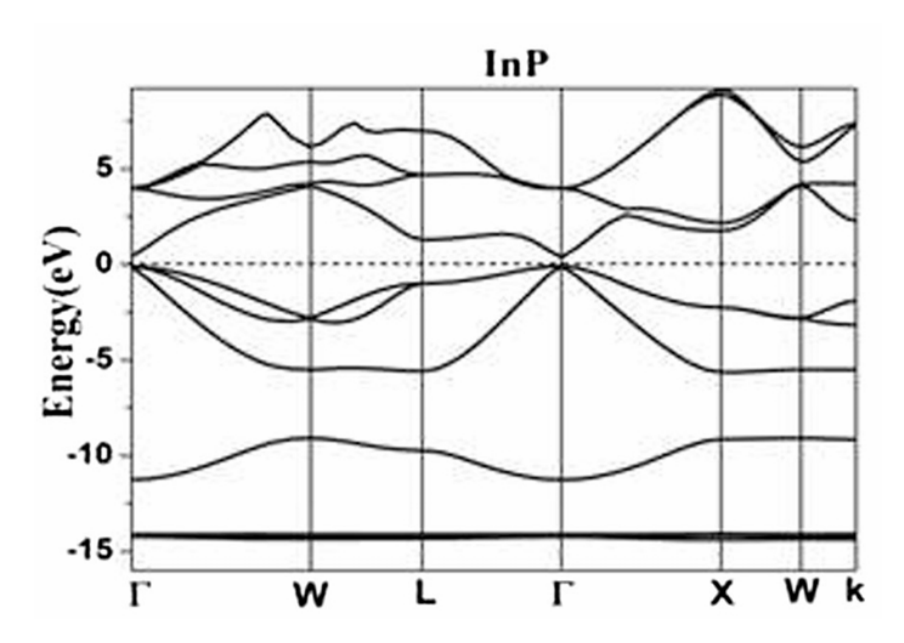


Figure 2.14: Electronic band structure of InP, referenced to the Fermi level (set to zero energy) [64].

2.4.3 Optical properties

It is widely recognized that the fundamental optical properties of semiconductors arise from electronic excitations within the crystal when they are exposed to an electromagnetic wave [65]. Figure 2.15 illustrates how the refractive index of InP varies with wavelength. At shorter wavelengths (around 0.25 μ m), the refractive index increases significantly and rapidly, reaching a prominent peak of approximately 4.4 in the violet/blue region of the spectrum (around 0.35 μ m).

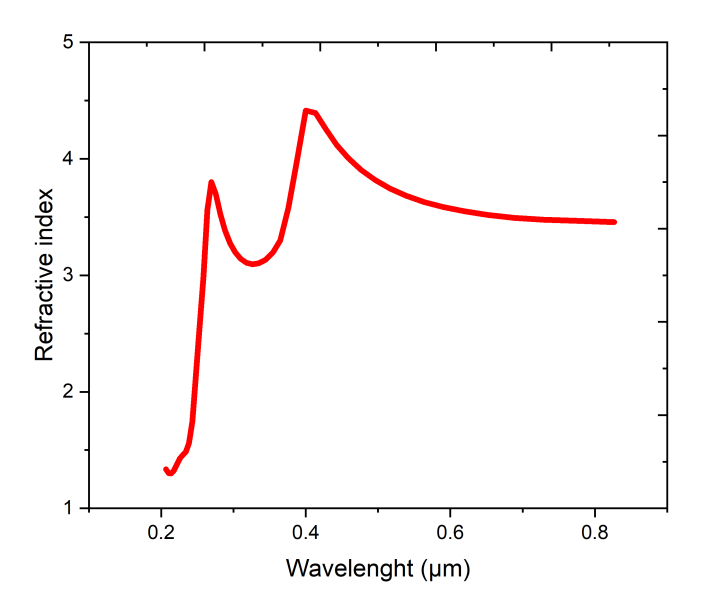


Figure 2.15: Refractive index of Indium Phosphide (InP) [66].

Figure 2.16 depicts the relationship between the absorption coefficient of InP and the wavelength of incident light. At shorter wavelengths, particularly below 0.3 µm (ultraviolet region), the absorption coefficient is very high, reaching a sharp peak around 0.25 µm with a value close to $1.8*10^6cm^{-1}$. This indicates that InP strongly absorbs ultraviolet light. As the wavelength increases into the visible (roughly 0.4 µm to 0.7 µm) and near-infrared (above 0.7 µm) regions, the absorption coefficient remains significantly lower, generally below $1*10^5cm^{-1}$ and further decreasing. This suggests that InP is more transparent to light in these longer wavelength ranges compared to the ultraviolet.

2.4.4 InP synthesis

Indium is recovered from fumes, dust, slags, and residues from zinc and lead–zinc smelting, then purified to high grades using classical chemical and electrochemical methods. It forms semiconducting compounds with non-metals like phosphorus. Indium phosphide is produced either by directly combining purified elements under

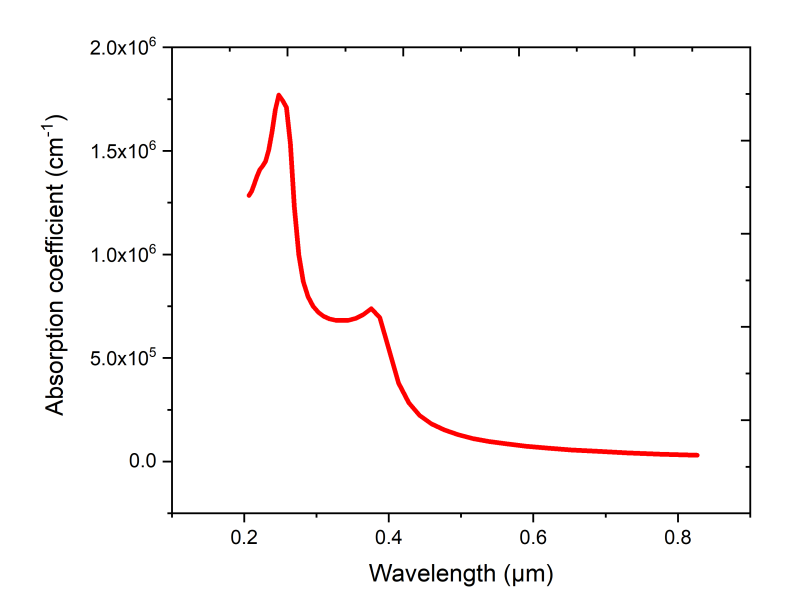


Figure 2.16: The absorption coefficient of Indium Phosphide (InP) [66].

controlled conditions or by thermal decomposition of a trialkyl indium compound with phosphine (PH_3) [67]. InP crystals are typically grown using the Liquid Encapsulated Czochralski (LEC) method [68], wich is the most commonly used method for manufacturing InP crystals.

2.4.4.1 Liquid Encapsulated Czochralski (LEC)

The schematic diagram of the growth system is shown in figure 2.17 .The process typically begins with a quartz container of about 40 mm in diameter, which is filled with high-purity indium and red phosphorus—both often available in 6-9s grade purity. The procedure is generally carried out in an argon gas atmosphere under high pressure, commonly around 60 atm .As the container is heated to temperatures between 200°C and 300°C, the solid red phosphorus sublimates into gas. This gas tends to condense on the cooler upper parts of the container, particularly near the neck, forming a liquid film that flows back down onto the molten indium and reacts with it at around 1000–1100°C, forming a melt of indium phosphide. This melt is often held for a period—about 50 minutes to ensure complete synthesis .During this phase, the crucible may be slowly lifted into a slightly cooler zone to create optimal conditions for crystal seeding. Once seeding starts, a (111)-oriented single crystal grows from the melt. A liquid phosphorus layer on the surface acts as an encapsulant to stabilize the melt and prevent contamination. The process is monitored in real time using TV and X-ray imaging [69].

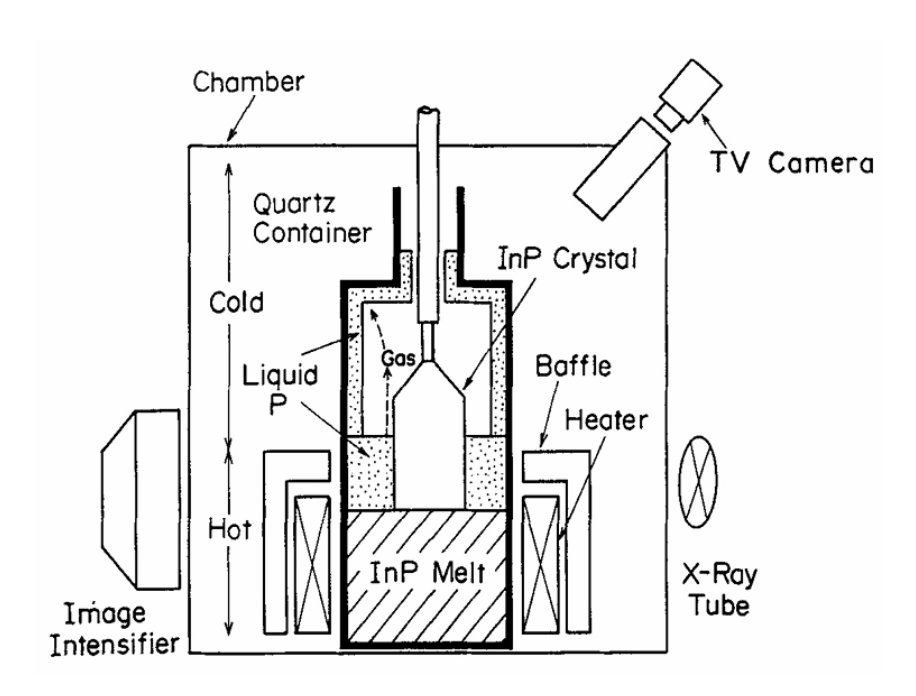


Figure 2.17: Diagram illustrating the furnace for the Liquid Encapsulated Czochralski method [69].

Chapter 3

Simulation and Results

Two-dimensional transition metal dichalcogenides (TMDs) exhibit chemically inert surfaces along their planes, free of dangling bonds, making them strong candidates for integration in nanoscale electronic and optoelectronic devices. Among these materials, molybdenum disulfide (MoS₂) has received considerable attention due to its direct band gap, which falls within the visible spectrum (1.8–1.9 eV). Despite these advantages, monolayer MoS₂ has demonstrated limited efficiency in optoelectronic applications, mainly because of its relatively poor light absorption. To overcome this limitation, researchers have increasingly focused on heterostructures that pair 2D TMDs with bulk III–V semiconductors, aiming to combine the unique electronic properties of 2D materials with the mechanical robustness and well-established performance of bulk semiconductors [70].

In this context, a MoS_2/InP based solar cell will be simulated based on the experimental work of Shisheng Lin et al. [71], with the aim of improving the cell's performance and evaluating its potential in photovoltaic applications. The study will focus on analyzing the effects of various material parameters, including the doping concentrations of both the emitter and absorber layers, their thicknesses, as well as the work functions of the front and back contacts. These simulations will be carried out using SILVACO TCAD software.

This chapter begins with a comprehensive introduction to the SILVACO TCAD simulation software, outlining its key features, an explanation of how to use ATLAS to simulate solar cells, focusing on the practical steps involved in constructing the MoS_2/InP solar cell model. This is followed by an in-depth presentation and analysis of the simulation results obtained for the simulated solar cell structure.

3.1 Silvaco's TCAD Software

SILVACO TCAD (Technology Computer-Aided Design from Silicon Valley Corporation) is a comprehensive simulation suite used for modeling semiconductor processes,

integrating various physics-based tools—such as ATHENA, ATLAS, MERCURY, and SSUPREM3 within a unified environment known as DECKBUILD. The software is capable of simulating a wide range of physical phenomena—including electrical, optical, and thermal behavior as well as technological processes involved in fabricating electronic components, such as deposition, etching, and doping through implantation or diffusion. These capabilities make it a valuable tool for optimizing fabrication parameters and predicting the performance of semiconductor devices, particularly solar cells [72,73]. In this study, device structures were created using DECKBUILD, simulations were carried out using ATLAS, and the results were visualized through TONY-PLOT.

3.1.1 DECKBUILD

It serves as the graphical interface that connects the user with the simulators. The interface is made up of two windows: one for creating and editing the input deck, where simulators can be invoked and managed using DECKBUILD commands, and another for displaying the outputs and results of the simulations [16].

3.1.2 ATLAS

ATLAS is a device simulation module based on physical principles, designed to predict the electrical characteristics of specific physical structures under given bias conditions. It accomplishes this by discretizing the device operation onto a grid. The carrier transport within the device is simulated by solving a set of differential equations, derived from Maxwell's equations, applied to this grid. This allows ATLAS to serve as a platform for analyzing AC, DC, and time-domain responses for all semiconductor technologies in both two and three dimensions [16].

3.1.3 TONYPLOT

TonyPlot is a graphical post-processing tool compatible with all SILVACO TCAD simulators and interactive environments like DeckBuild, VWF, and SPDB. It offers extensive features for visualizing and analyzing simulation results. The tool supports various types of plots, such as 2D and X-Y graphs, polar and Smith charts, cross-sectional views, and RSM plots in 1D, 2D, and 3D formats, along with statistical plots. Users can also load and overlay multiple files within a single plot for comparison purposes. Additionally, TonyPlot includes tools like 1D cross-sections from 2D plots, measurement rulers, probes, integrators, and more [74].

3.2 Simulation by ATLAS

ATLAS is a physics-based device simulator used to predict the electrical behavior of devices by analyzing their physical structure and applied bias conditions. It operates by simultaneously solving the Poisson equation (3.1) along with the continuity equations for electrons (3.2) and holes (3.3) ,which are given by the expressions below [72]:

$$\frac{d^2}{dx^2}\psi(x) = -\frac{q}{\epsilon_0 \epsilon_r} (p(x) - n(x) + Nd(x) - Na(x))$$
(3.1)

$$\frac{\partial n}{\partial t} = \left(\frac{1}{q}\right) \frac{\partial Jn}{\partial x} - Rn + G \tag{3.2}$$

$$\frac{\partial p}{\partial t} = -\left(\frac{1}{q}\right)\frac{\partial Jp}{\partial x} - Rp + G \tag{3.3}$$

These equations form the core framework for simulating electronic devices. In this process, a grid is laid over the device, and each node on the grid is governed by differential equations derived from Maxwell's laws and semiconductor transport principles. Silvaco-ATLAS processes input files through the DeckBuild interface.

The input file contains code that initiates ATLAS using the command "Go Atlas" [72]. Every ATLAS command consists of a main keyword followed by a group of parameters. The general format is as follows [16]:

After this command, the sequence of instructions in the input file becomes crucial. Maintaining the correct order is essential for ATLAS to properly apply all the specified models and settings [16,72]. The order of commands in ATLAS is as follows:

3.2.1 Structure specification

The structure is specified by defining the mesh, regions, electrodes, and doping levels.

3.2.1.1 Mesh

To describe a device structure using the Atlas command language, the first step is to create a mesh. This mesh is formed by horizontal and vertical lines spaced according to user-defined intervals. These lines generate a network of triangles that define the physical boundaries of the simulation region. A node is placed at each corner of these triangles, and the simulation calculates the relevant equations at each of these nodes [72].

The general format to define a mesh is:

MESH SPACE.MULT=<VALUE>

X.MESH LOCATION=<VALUE> SPACING=<VALUE> Y.MESH LOCATION=<VALUE> SPACING=<VALUE>

Mesh design is essential for accurate simulation results. A coarse mesh speeds up computation but reduces accuracy, while a fine mesh slows it down yet provides more precise outcomes. The most efficient strategy is to apply a fine mesh only in critical regions—such as near junctions, depletion zones, areas with strong electric fields, significant current flow, high recombination, or intense impact ionization—while using a coarser mesh in less critical areas [72,73,75].

3.2.1.2 **Region**

Once the mesh is defined, the next step is to specify the regions. The format for defining the regions is as follows [75]:

REGION number=<integer> <material type> <position parameters>

3.2.1.3 Electrodes

In this step, the device's electrodes are specified using the ELECTRODE statement, which is applied as follows [72]:

ELECTRODE NAME=<electrode name><position parameters>

3.2.1.4 Doping

The final aspect of the structure specification to be defined is the doping, it can either be of type N or P, and the distribution can be either uniform or Gaussian. Doping is specified using the DOPING statement, as illustrated below [73]:

DOPING <distribution type> <dopant type> <position parameters>

3.2.2 Materials and Models Specification

Once the structure specification is defined, the next step is to specify materials and models.

3.2.2.1 Material

We use the MATERIAL statement to define key parameters and material properties for use in the simulation. A range of characteristics can be specified for the material assigned to a particular region, including—among others—carrier lifetimes, electron and hole mobilities, electron affinity, dielectric constant, bandgap energy, and an optical file that provides the wavelength-dependent refractive index (n) and extinction coefficient (k) [72].

The ATLAS format of the material statement is as follows:

MATERIAL < localization > < material definition >

Since MoS_2 is not included in the Silvaco material database, we manually defined its properties as follows:

MATERIAL material=MoS2 index.file=MoS2.nk EG300=1.8 affinity=4 NC300=1.08e13 NV300=1.19e13 permittivity=6.82 mun=60 mup=20 user.group=semiconductor user.default=si out.index=RMoS2new

3.2.2.2 Models

To achieve realistic simulation results, it is important to consider various complex dependencies of device properties. However, in some cases, these complexities may not be essential. To reduce computational load, ATLAS offers separate models for each individual property dependence, allowing users to activate them selectively. The accuracy of the simulation outcomes depends on the specific models employed [16].

The models are activated in ATLAS as follows [72]:

MODELS < model-name >

In our simulation we define models as follows:

MODELS bipolar temperature=300 print

3.2.2.3 Contact

The 'contact' statement instructs ATLAS on how to handle the electrode. By default, electrodes in contact are assumed to be Ohmic. However, if the electrode is intended to behave as a Schottky contact, the corresponding work function must be specified [16]. The contact syntax is as shown below [73]:

CONTACT name = < name >

3.2.3 Numerical Methods Selection

Several numerical approaches can be used to solve semiconductor device problems. SILVACO-ATLAS utilizes three distinct solution techniques [75]:

• GUMMEL method:

The first approach is the GUMMEL method, which is effective for systems with weakly coupled equations but only achieves linear convergence. In this technique, each variable is solved sequentially while holding the others fixed at their latest computed values. This cycle repeats until a stable solution is found. Although GUMMEL iteration can handle poor initial guesses, its convergence rate is relatively slow [16].

•NEWTON method:

The NEWTON method is used for systems with strong coupling between equations and offers quadratic convergence. However, in ATLAS, this can result in longer com-

putation times when dealing with variables that are nearly constant or only weakly coupled [16,72].

• BLOCK method:

This method integrates both the GUMMEL and NEWTON approaches, making it effective for solving systems that contain a mix of equation types [73].

A combined approach may be used, starting with the GUMMEL method and switching to BLOCK or NEWTON if convergence is not reached within a set number of iterations [16]. For example:

METHOD GUMMEL NEWTON

3.2.4 Solution Specification

After defining all necessary parameters, the simulation proceeds to the solution stage in ATLAS, which includes four key sections: LOG, SOLVE, OUTPUT, and SAVE [72].

3.2.4.1 "LOG"

The Log statement is used to save all terminal characteristics into a data file. Any DC, transient, or AC data produced by the Solve command following a Log instruction will be recorded [16,73,75]. The example below illustrates how to use the Log command: LOG OUTFILE=mos2.LOG

3.2.4.2 "SOLVE"

The SOLVE statement is used to compute the solution for one or more DC or AC bias points. To obtain an initial approximation of the final result, a simplified preliminary solution—typically solving only Poisson's equation—is performed [72]. The syntax for this is as follows:

SOLVE INIT

SOLVE VANODE=0 VSTEP=0.1 VFINAL=0.9 NAME=ANODE

3.2.4.3 "LOAD" and "SAVE"

To improve the accuracy of initial guesses for bias points, the "Save" and "Load" statements are used together. The SAVE statement stores all data related to the node points, while the LOAD statement later retrieves this information to assist in solving the device [72].

The following example shows a 'save' statement that stores the data into a file named "mos2":

SAVE outf=mos2.str

3.2.5 Extraction and Plotting data

The EXTRACT command enables the extraction of device parameters, allowing electrical quantities such as short-circuit current (Jsc), open-circuit voltage (Voc), efficiency (η), and others to be derived from simulation results. Its syntax is as follows:

EXTRACT INIT INF = "<file name>"

The EXTRACT command operates on a previously solved curve or structure file. By default, it uses the currently active log file unless a different filename is specified prior to the extraction process. All device simulation results in ATLAS are visualized by first saving them to a file, which is then loaded into TonyPlot for plotting using the TONYPLOT command [72,73].

3.3 Results and Discussion

In this section, we present the simulation results of the MoS_2 /InP solar cell. as illustrated in Figure 3.1, The device structure includes a single layer of MoS_2 functioning as the emitter, an indium phosphide (InP) wafer serving as the absorber, and aluminum (Al) and gold (Au) used as the front and rear electrodes, respectively. All the parameters used of these materials were obtained from various theoretical and experimental literature sources, and they are presented in table 3.1. The current-voltage characteristics of the heterostructure solar cell were measured under AM 1.5G conditions with an illumination intensity of $0.1W/cm^2$.

Table 3.1: Input parameters of the Materials Used.

Property	MoS2	InP
Thickness(µm)	0.00072 [76]	350
BandGap(eV)	1.8 [71]	1.35
Electron Affinity(eV)	4	4.4
Dielectric permittivity(ε_r)	6.82	12.5
CB effective density of State(cm^{-3})	10^{19}	$5.68 * 10^{17}$
VB effective density of State(cm^{-3})	$9*10^{20}$	$8.87 * 10^{18}$
Electron mobility($cm^2V^{-1}s^{-1}$)	60 [77]	4600
Hole mobility($cm^2V^{-1}s^{-1}$)	10	150
Donor/acceptor	$3.36 * 10^{16}$ [78]	$2*10^{18}$ [71]
density $(N_D/N_A)(cm^{-3})$		
Contact Property	Al	Au
Thickness(µm)	0.1 [71]	0.06 [71]
WorkFunction(eV)	4.28	5.1

To enhance the overall performance of our solar cell, this study will investigate the effects of doping concentration in both the absorber and emitter layers, the thickness

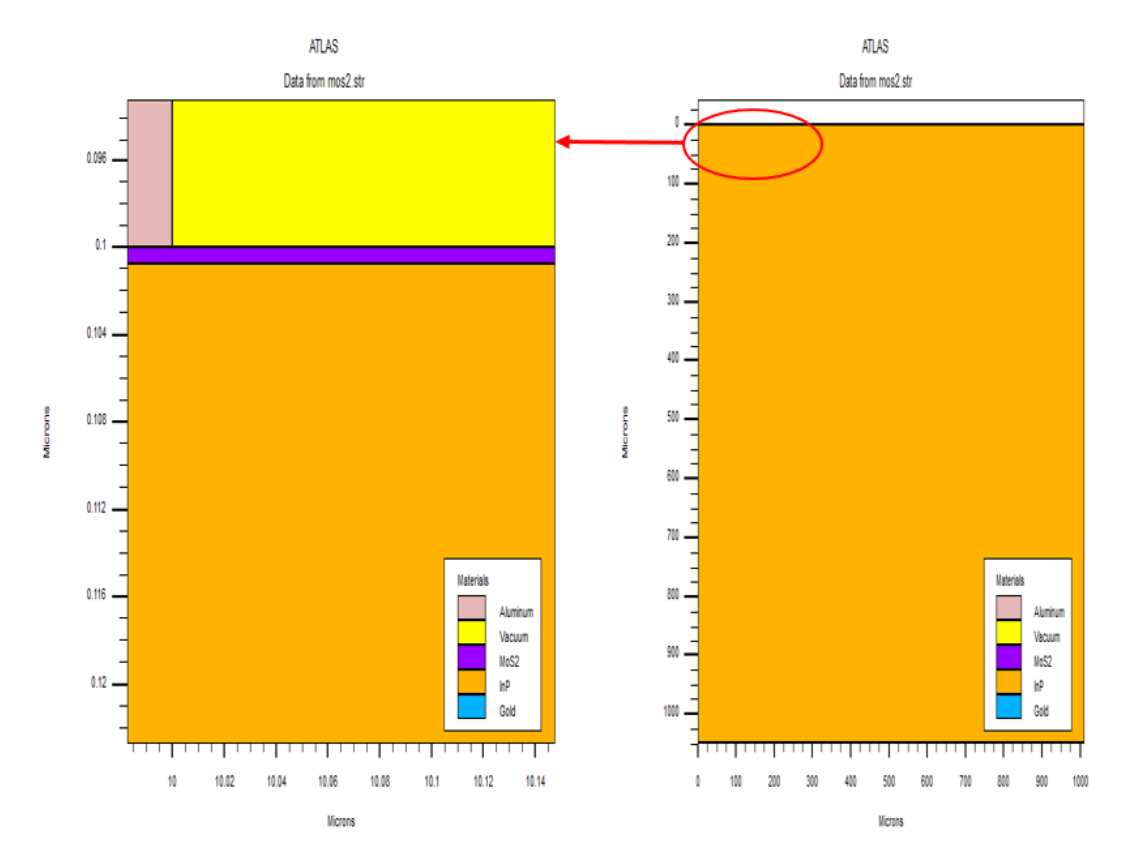


Figure 3.1: The simulated structure of the MoS₂/InP solar cell.

of these layers, and the work functions of the anode and cathode. In each simulation, only the parameter under investigation will be altered, while all other parameters are maintained at their previously optimized values.

3.3.1 Effect of Absorber Layer Doping Concentration

The simulation begins with analyzing the impact of varying the doping concentration of the absorber layer (InP), ranging from 10^{13} to 10^{19} cm⁻³ [79], while all other parameters are held constant at their initial values specified in table 3.1. The obtained results consist of the JV curve and the solar cell parameters presented in Figures 3.2 and 3.3, respectively, including the short-circuit current density (Jsc), open-circuit voltage (Voc), fill factor (FF), and power conversion efficiency (PCE).

As observed in Figure 3.2,the doping concentration in InP layer exhibits a notable influence on the JV curve of the solar cell. The experimental curve was taken from the report by Lin Shisheng et al. [71],in which an InP doping concentration of $2*10^{18}cm^{-3}$ was employed.When we applied the same doping level, we did not achieve identical results;however, a comparable outcome was observed when the doping concentration was reduced to $1.68*10^{13}cm^{-3}$. This discrepancy may be attributed to the incomplete removal of the native oxide layer on the surface of the InP substrate.

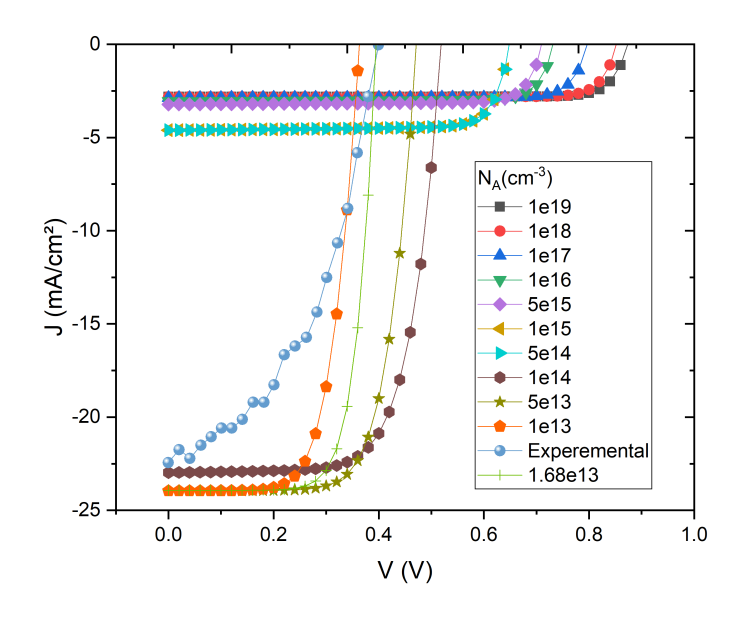


Figure 3.2: Variation of the JV Curve with InP Doping Concentration.

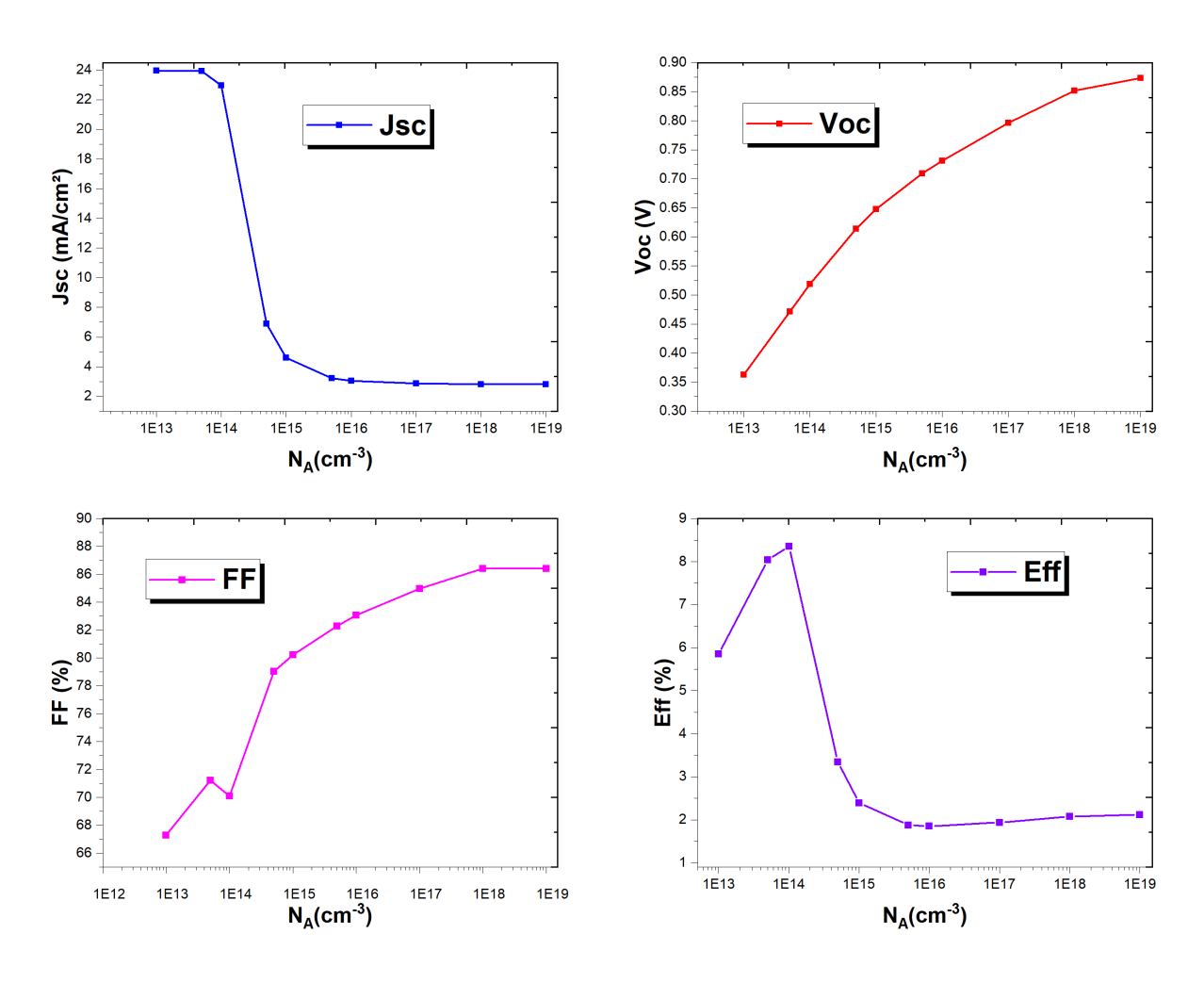


Figure 3.3: Solar cell parameters as a function of InP doping concentration.

In figure 3.3 a sharp decrease in the short-circuit current density (Jsc) is observed. This behavior can be attributed to that Increased doping narrows the depletion region, which means fewer photons are absorbed within that region, and fewer photogenerated electrons are collected efficiently. While the Voc is increasing due to the increase in the built-in potential (Vbi) of the junction. As a result, it is observed that the efficiency increases at doping concentrations below $10^{14}cm^{-3}$, owing to the Jsc remaining nearly constant within this range while the Voc continues to rise. However, above this concentration, a sharp decline in efficiency is evident, mainly due to the significant reduction in the Jsc. In contrast, the fill factor (FF) continues to increase, which can be attributed to a reduction in series resistance and improved carrier transport, which enhance the shape of the IV curve and allow for more efficient power extraction near the maximum power point. The best result was obtained at a doping concentration of $10^{14} cm^{-3}$.

3.3.2 Effect of Emitter Layer Doping Concentration

This study focuses on investigating the impact of emitter layer doping density. This will be done by varying the doping concentration from $3.36*10^{16}cm^{-3}$ to $2.5*10^{20}cm^{-3}$ [78, 80], the doping concentration of InP will be fixed at its optimal value obtained in the previous analysis ($N_A = 10^{14}cm^{-3}$), while keeping all other parameters constant at their initial value. The results obtained are presented in figure 3.4 and 3.5 which illustrate the JV curve and the cell parameters, respectively.

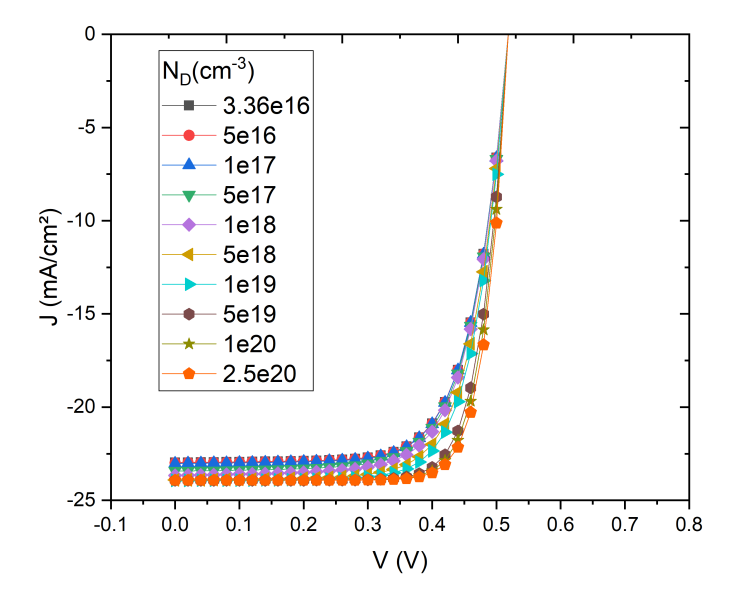


Figure 3.4: Variation of the JV Curve with MoS_2 doping concentration.

The JV curve shows only slight changes with increasing donor concentration. This can

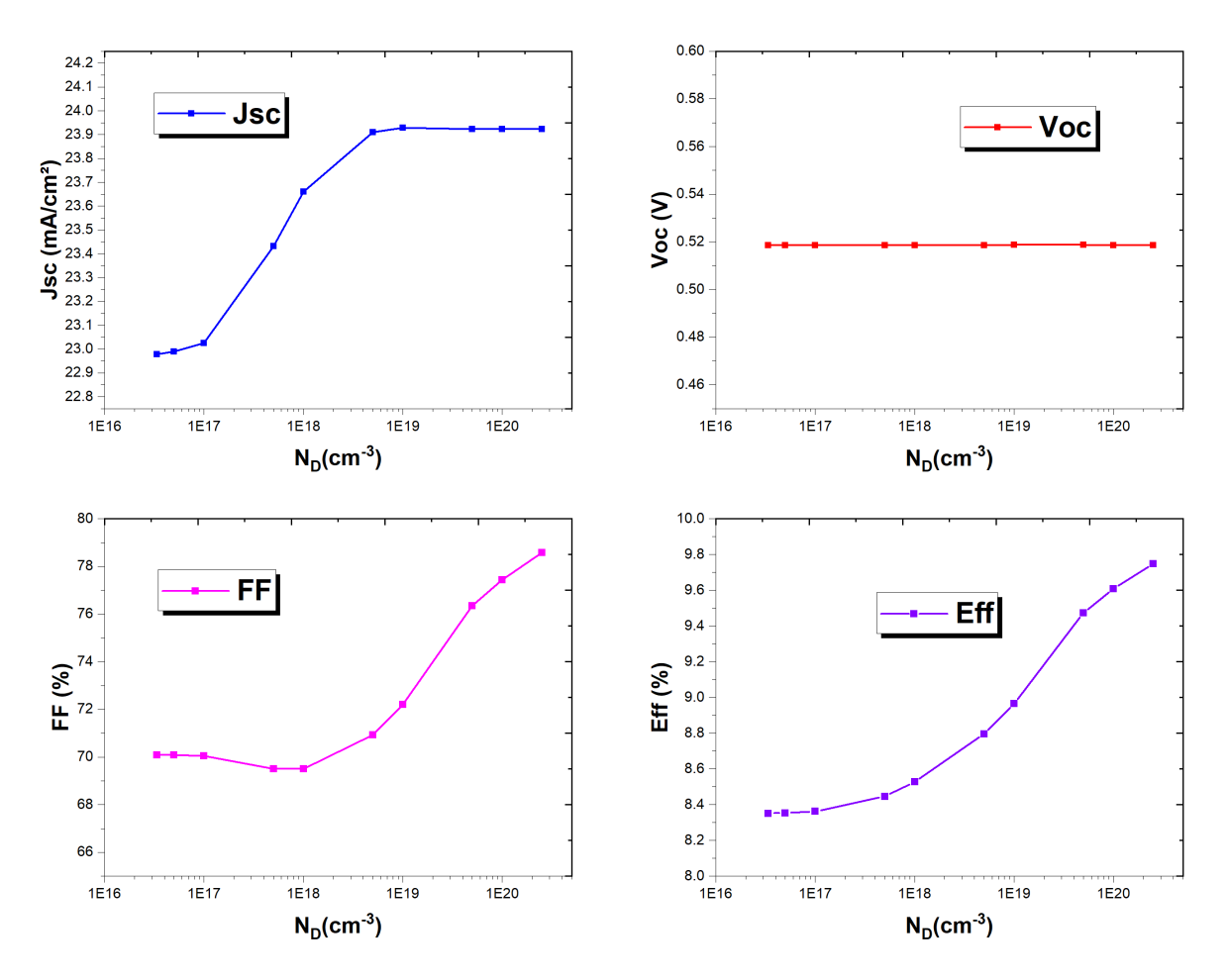


Figure 3.5: Solar cell parameters as a function of MoS_2 doping concentration.

be observed in the increase of Jsc as the doping concentration increases. This is likely due to the enhanced extension of the space-charge region into the p-type layer, where optical absorption primarily occurs. This Leads to more efficient carrier separation and, as a result, increases the short-circuit current. Consequently, the efficiency also increases, since the Voc remains constant, which can be explained by the band diagram illustrated in figure 3.6. It is observed that at low doping concentrations, a significant discontinuity appears at the barrier. As the doping concentration increases, this discontinuity is reduced. However, the barrier width remains essentially unchanged in both cases. The fill factor also increases due to the reduction in series resistance caused by the increased number of charge carriers. The highest efficiency was obtained at a donor concentration of $2.5*10^{20}cm^{-3}$.

3.3.3 Effect of Absorber layer thickness

In this step, the effect of InP layer thickness on the cell performance will be investigated, while keeping the doping concentrations fixed at the optimal values obtained previously ($N_A = 10^{14} cm^{-3}$, $N_D = 2.5 * 10^{20} cm^{-3}$). The thickness will be varied from

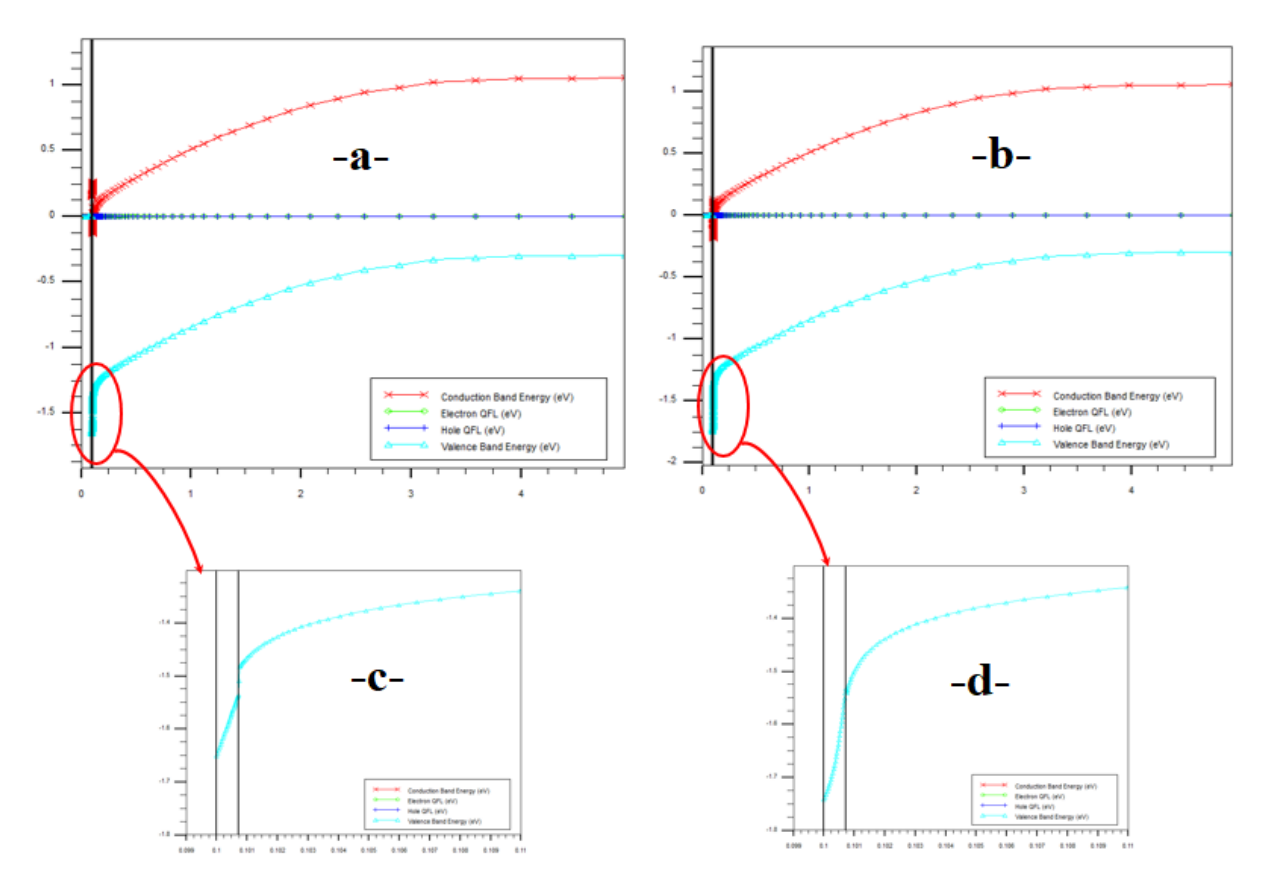


Figure 3.6: Energy band diagrams of MoS_2 under different donor doping concentrations: (a) and (b) show the full spatial profiles for low and high donor doping, respectively. Insets (c) and (d) provide zoomed-in views near the surface.

350 to 3000 μm , while the other parameters remain constant. The corresponding results are illustrated in Figures 3.7 and 3.8.

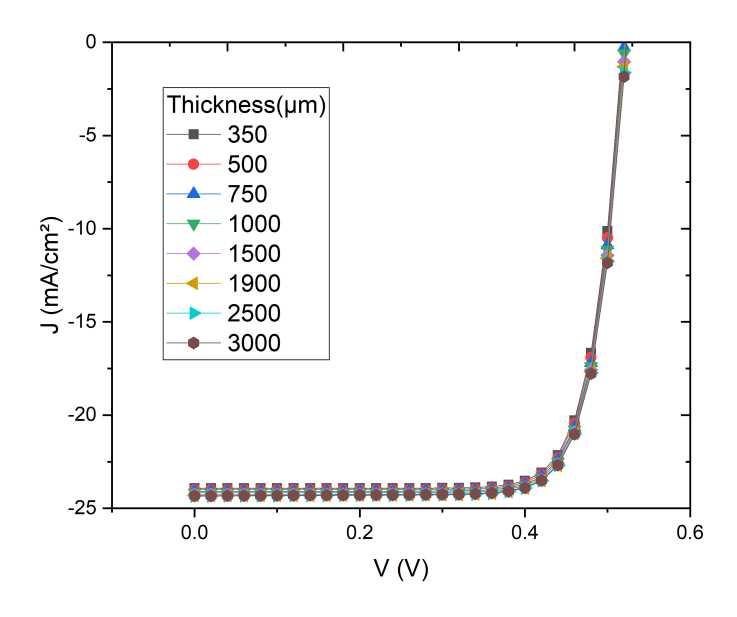


Figure 3.7: Variation of the JV Curve with InP thickness.

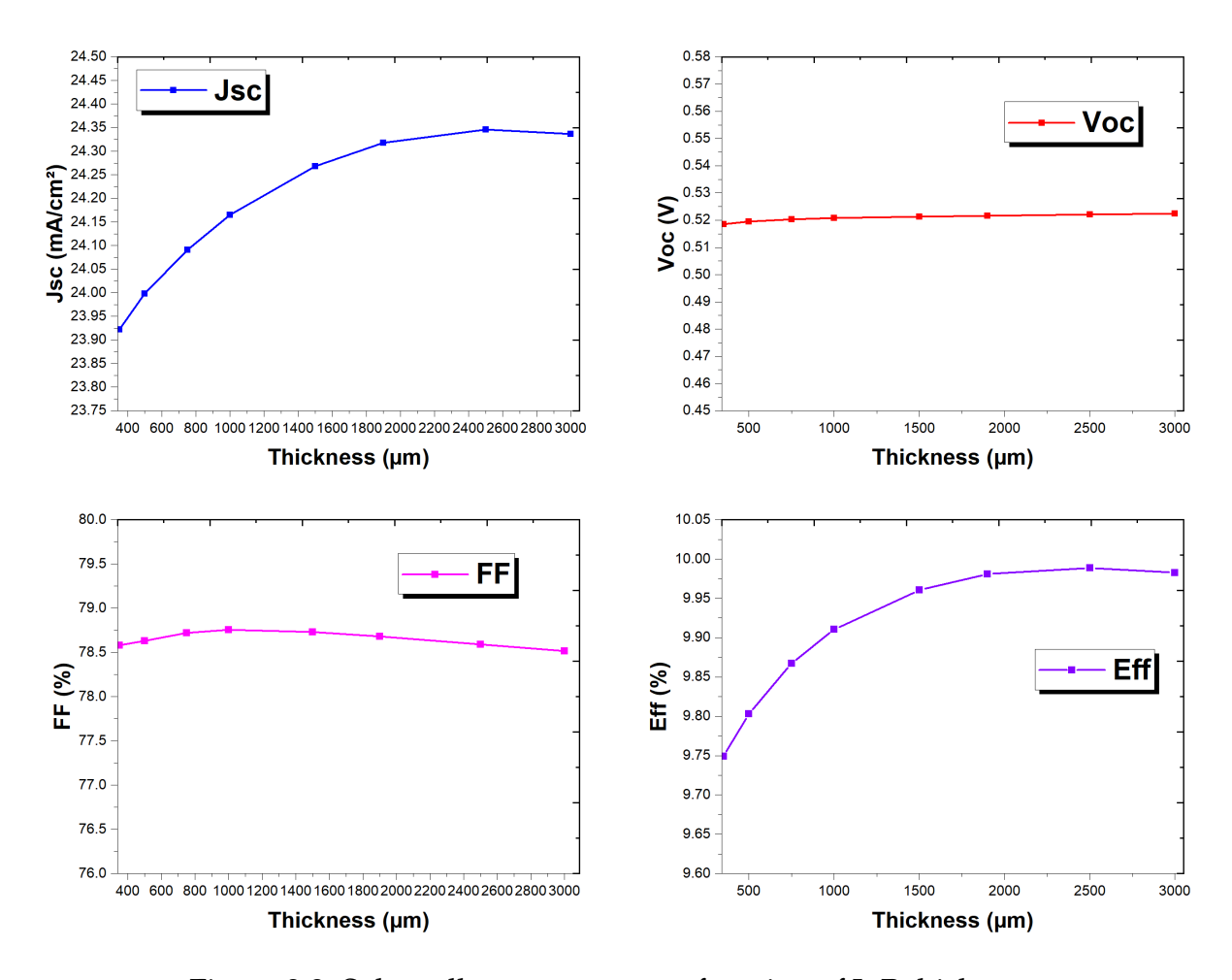


Figure 3.8: Solar cell parameters as a function of InP thickness.

Figure 3.7 presents the JV curve in different InP thicknesses indicating an almost negligible change. Meanwhile, as shown in Figure 3.8, the Jsc increases due to the enhanced absorption of incident photons, particularly those with longer wavelengths. Similarly, the efficiency shows the same behavior, while Voc remains constant.

The thickness that yielded the highest efficiency is 2500 μm .

3.3.4 Effect of Emitter layer thickness

It is important to study the effect of MoS_2 layer thickness on our solar cell performance. This can be assessed by comparing device behavior across monolayer, bilayer, trilayer, and bulk structures. This involves varying the thickness along with the corresponding changes in bandgap as defined in table 3.2 and the n-k profile as well. This is done while keeping the doping concentrations and InP thickness at their optimal values, along with keeping the other parameters constant. The J–V characteristics of the cell and its parameters under different MoS_2 layer conditions are presented in Figures 3.9 and 3.10, respectively.

Table 3.2: MoS₂ properties depending on the number of layers.

	Monolayer	Bilayer	Trilayer	Bulk
Thickness(nm)	0.72	1.44	2.16	4000
Bandgap(ev)	1.8	1.53 [81]	1.46 [82]	1.2

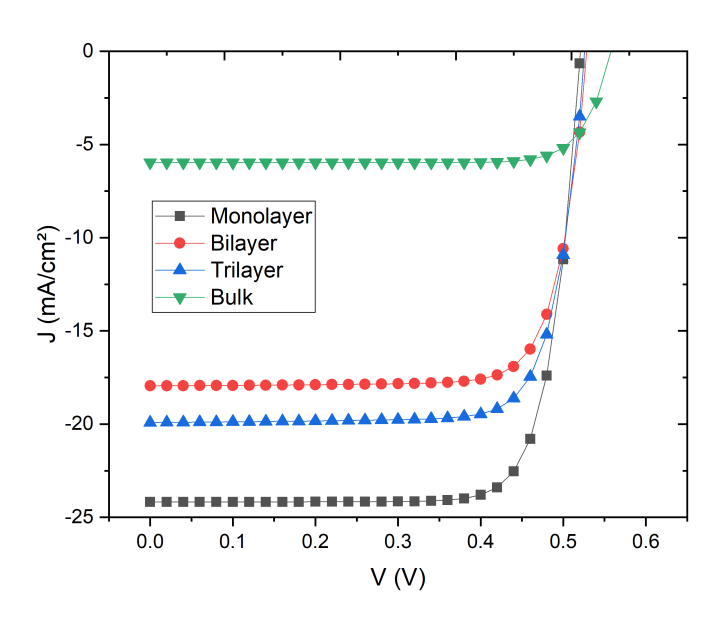


Figure 3.9: Variation of the JV Curve with MoS_2 thickness.

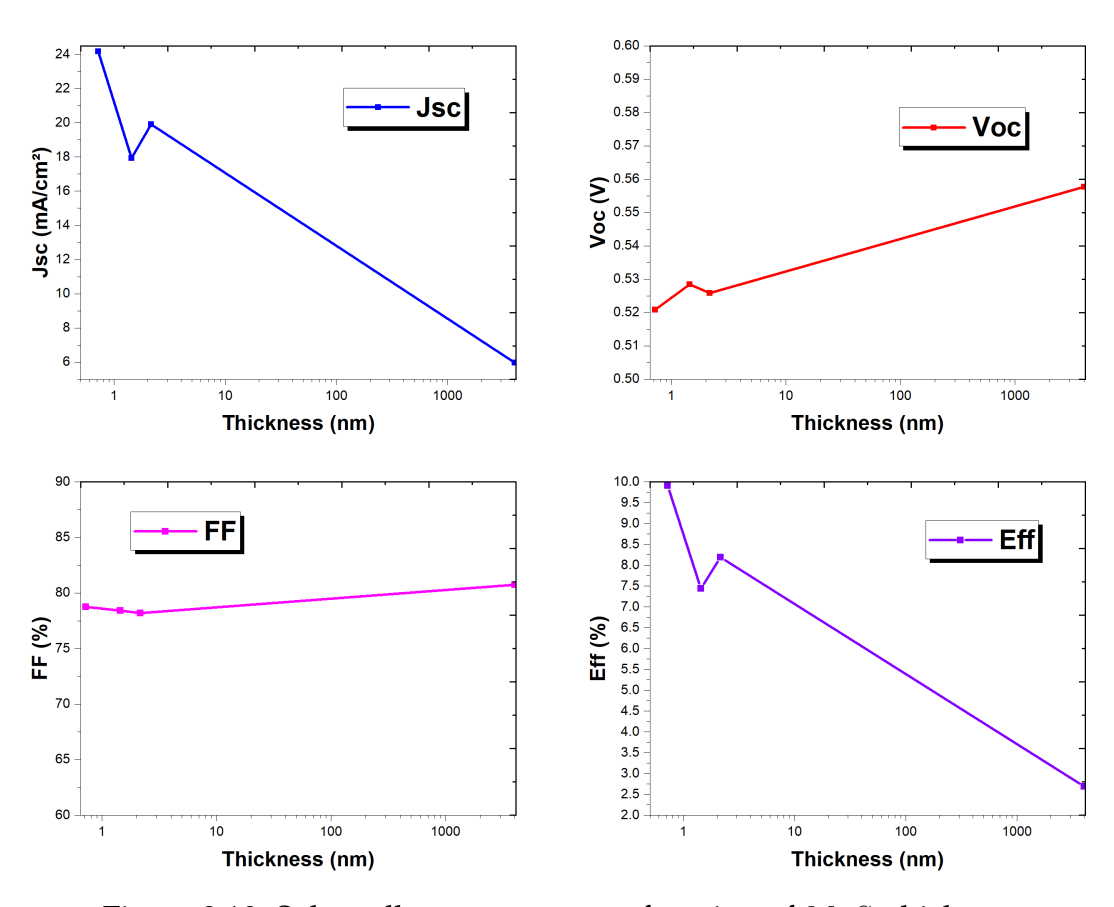


Figure 3.10: Solar cell parameters as a function of MoS_2 thickness.

From Figure 3.10, it is evident that the short-circuit current decreases significantly as a result of the increased thickness, which moves the space-charge region away from the surface and thus reduces carrier collection. On the other hand, the Voc shows a slight increase, which may be attributed to the change in bandgap. While the efficiency is strongly influenced by the Jsc ,showing the same behavior. However, in the case of the trilayer, a different behavior is observed. This is due to the fact that the absorption of the trilayer is higher compared to the bilayer and figure 3.11 confirms this observation.

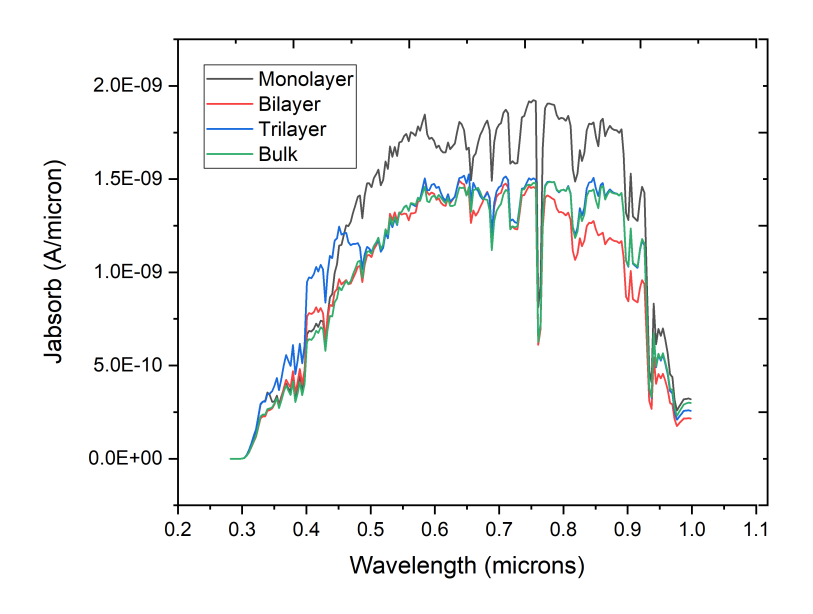


Figure 3.11: Photon absorption quantified as photocurrent (Jabsorb) in MoS₂ for Different Layer Thicknesses.

3.3.5 Impact of Back Contact Work Function

Since it plays a major role in determining device efficiency, this study investigates the influence of the back contact work function on device performance by varying its value from 4.6 to 5.65 eV [83], while maintaining the optimal parameters identified in previous studies. Figures 3.12 and 3.13 display the obtained current-voltage behavior and the key output parameters of the solar cell, respectively.

As observed in Figure 3.13,increasing the work function of the back contact enhances the overall performance of the solar cell, as all parameters show enhancement. This improvement is attributed to the reduction of the Schottky barrier at the metal/InP interface at higher work function values, enabling more efficient hole transport to the rear electrode. However, the short-circuit current saturated at work function values higher than 5.1 eV. This is likely because the contact becomes ohmic at that stage, meaning that further increases in the work function do not improve charge extraction since it has already reached an optimal level.

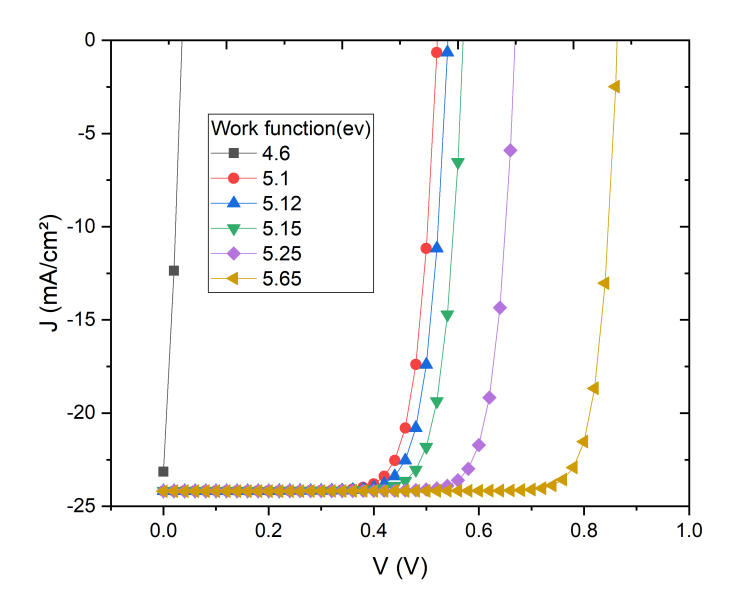


Figure 3.12: JV characteristic in various back contact work functions.

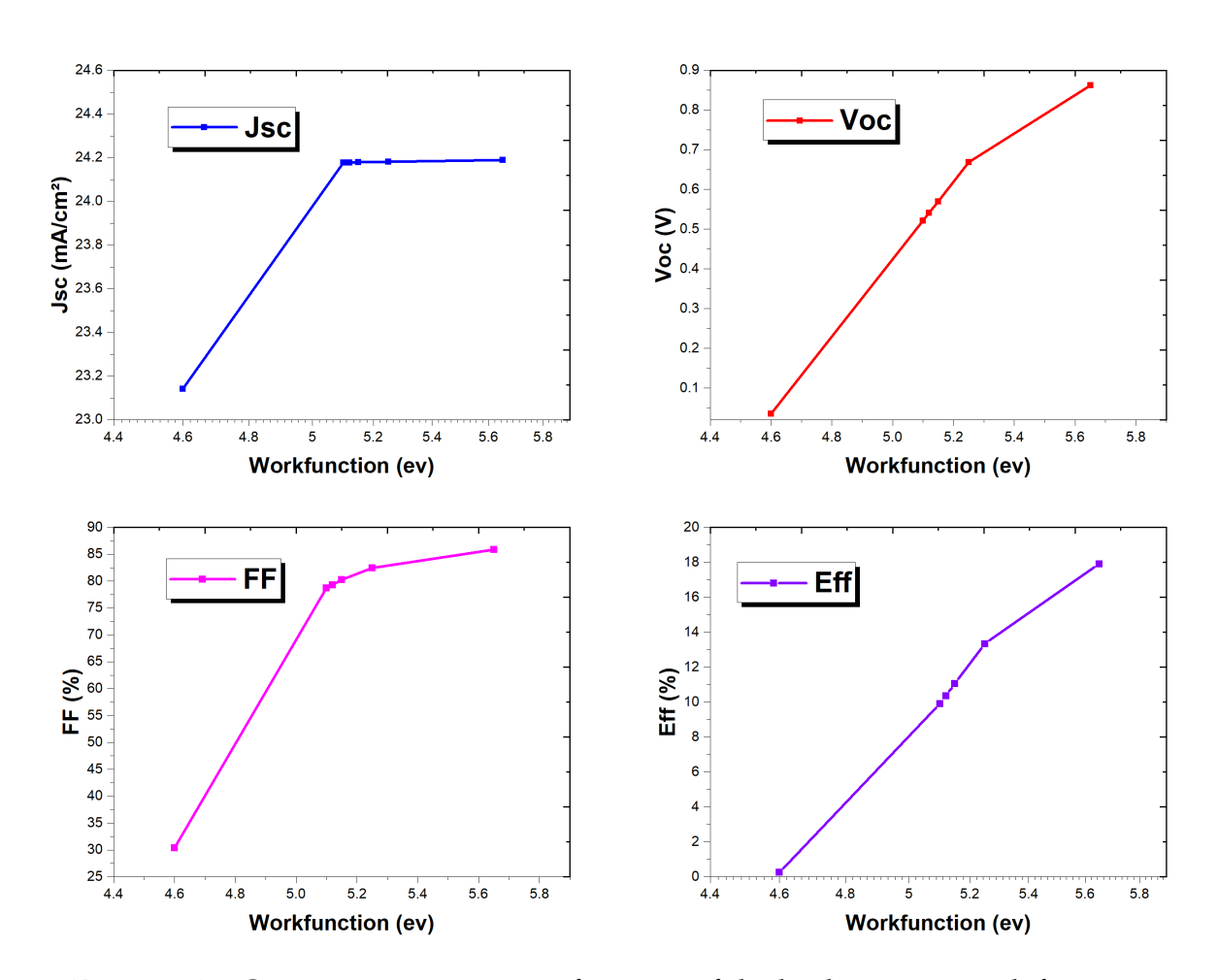


Figure 3.13: Output parameters as a function of the back contact work function.

The best device performance was achieved at a work function of 5.65 eV, which corresponds to Platinum metal.

3.3.6 Impact of Front Contact Work Function

In this part we explore the influence of the front contact work function after fixing the optimal parameters obtained from previous optimizations. To assess its effect, The front contact work function will be varied from 3.7 to 5.25 eV [83,84].

The resulting current-voltage characteristic and the main performance parameters of the solar cell are presented in figures 3.14 and 3.15, respectively.

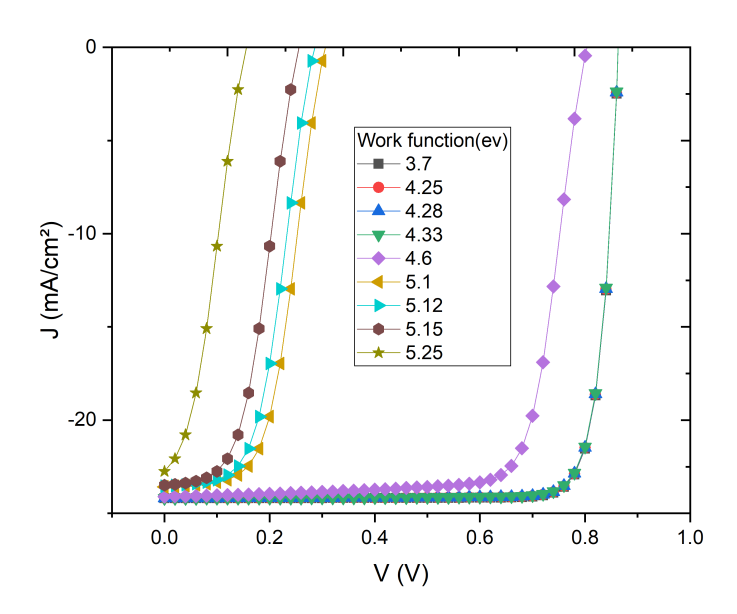


Figure 3.14: JV characteristic in various front contact work functions.

From the (J-V) curves illustrated in figure 3.14,it is clear that the front contact work function plays a critical role in the performance of the solar cell, as shown in Figure 3.15, all the solar cell parameters exhibit a decline at front contact work function values exceeding 4.3 eV. This degradation is attributed to the formation of a Schottky barrier at the MoS_2 /front electrode interface, which limits electron transport, as well as an increase in series resistance.

The cell exhibits optimal performance when the work function of the front electrode is 3.7 eV, which corresponds to Magnesium metal.

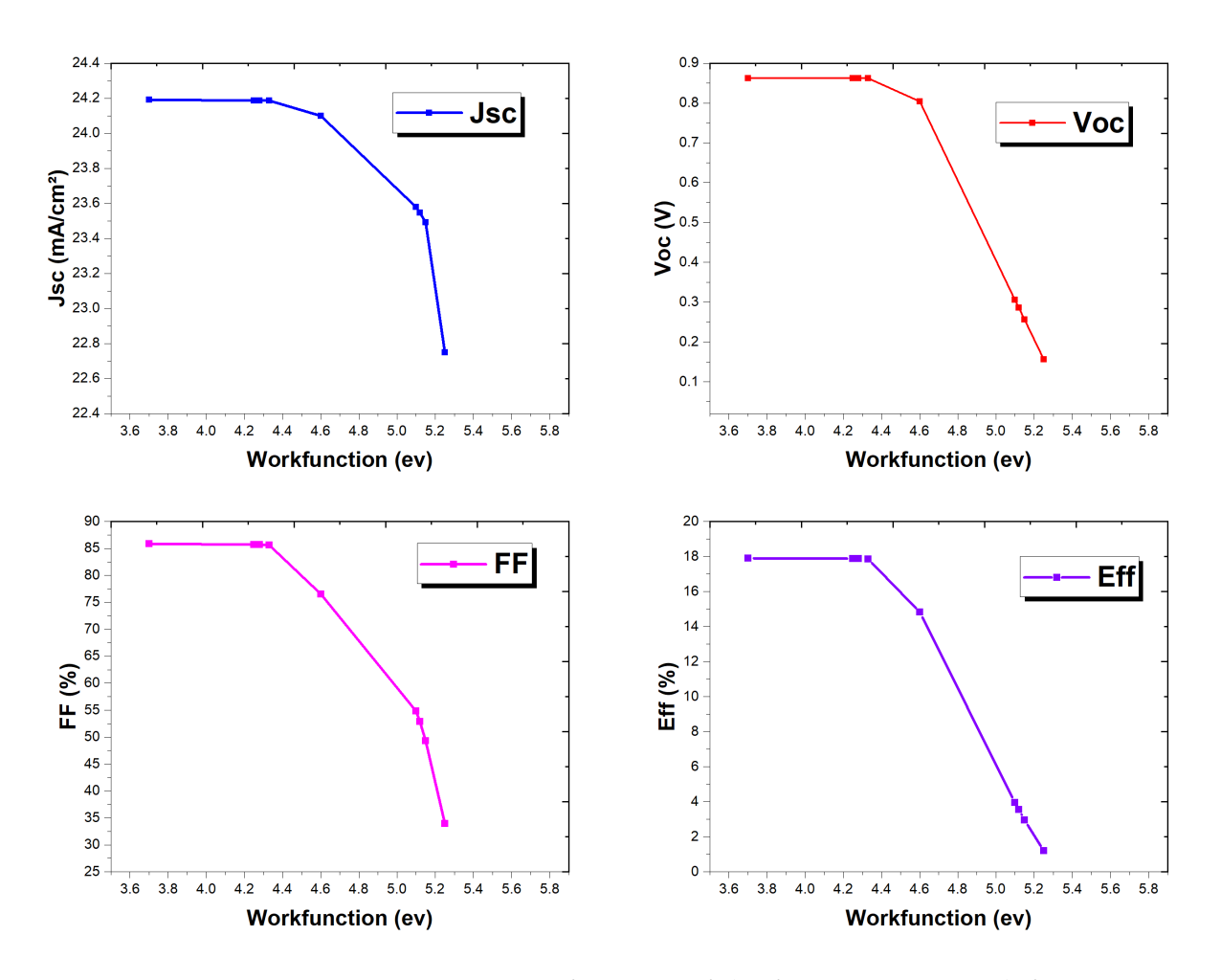


Figure 3.15: Output parameters as a function of the front contact work function.

3.4 Final Results

The performance of the MoS_2/InP heterojunction solar cell is simulated and analyzed, examining the effects of the doping concentration and thickness of the MoS_2 emitter layer and InP absorber layer, along with the work function of both the front and back contacts. Based on the simulation results, the optimal thickness for the InP absorber layer is determined to be 2500 μ m, with a doping concentration of $10^{14}cm^{-3}$. For the MoS_2 emitter layer, the best performance is achieved with a thickness of one atomic layer (0.72 nm) and a doping density of $2.5*10^{20}cm^{-3}$. The front contact work function is optimized at 3.7 eV, while the optimal back contact work function is found to be 5.65 eV.

Figure 3.16 illustrates the final current-voltage (J–V) response of the optimized MoS_2/InP solar cell, with its key performance metrics presented in Table 3.3.

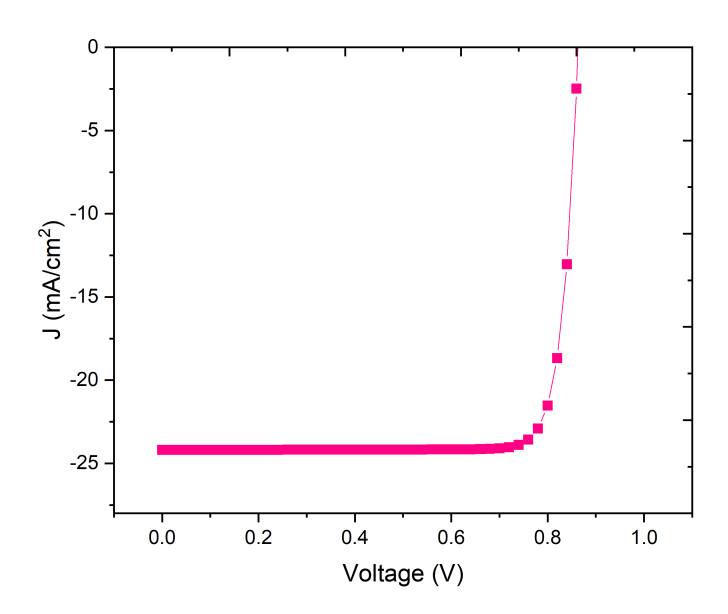


Figure 3.16: J-V characteristic of The optimized cell.

Table 3.3: Best obtained performance.

Jsc(mA/cm ²)	Voc(V)	FF(%)	Eff(%)
24.191	0.86271	85.8564	17.918

Conclusion

This thesis has investigated the application of molybdenum disulfide (MoS₂), a prominent two-dimensional material, in the design and optimization of advanced solar cells, with a particular focus on its electronic ,optical and structural properties and photovoltaic performance. As a member of the transition metal dichalcogenide (TMD) family, MoS₂ offers unique properties such as a direct band gap in monolayer form and excellent optical absorption, making it a highly attractive candidate for next-generation photovoltaic devices.

The performance of the MoS₂/InP heterojunction solar cell is simulated and analyzed using SILVACO TCAD, with a focus on the effect of the MoS₂ emitter, the InP absorber, and both the front and back contacts. Simulation results show that the thickness and doping concentration of the InP absorber significantly influence light absorption and carrier generation, directly impacting current output. A lower doping concentration in the InP absorber enhances the depletion width and carrier collection efficiency, while a higher doping level in the MoS₂ emitter improves junction quality and facilitates efficient charge separation. The MoS₂ emitter layer affects the junction quality and charge carrier separation, with its properties playing a key role in device performance; notably, the monolayer structure exhibits the best overall efficiency. The front contact work function affects the barrier height at the interface and influences electron injection and collection, while the back contact work function is critical for efficient hole extraction. Optimizing these parameters collectively leads to a noticeable improvement in the overall power conversion efficiency of the device. After applying all of the optimal properties obtained, the resulting device exhibited the following performance values: Voc of 0.86271 V, Jsc of 24.191 mA/cm², FF of 85.8564 % and PCE of 17.918 %. In conclusion, the results of this study highlight the growing importance of incorporating two-dimensional (2D) materials, particularly MoS₂, in the development of nextgeneration solar cells. These materials exhibit exceptional electronic and optical properties, making them strong candidates for enhancing the efficiency and performance of photovoltaic devices. Integrating 2D materials into the design of nanoscale solar cell architectures opens new horizons for lightweight, flexible, high-efficiency, and lowcost devices. Due to their atomically thin nature, 2D materials require minimal material usage, which reduces raw material costs. Additionally, many 2D materials can be

synthesized using scalable and solution-based methods, such as chemical vapor deposition (CVD) or liquid-phase exfoliation, which are compatible with low-temperature, low-energy, and cost-effective fabrication processes. Therefore, continued research in this field, through both simulation and experimental studies, is essential to push this technology closer to large-scale commercial application.

Bibliography

- [1] M. V. Dambhare, B. Butey, and S. V. Moharil, "Solar photovoltaic technology: A review of different types of solar cells and its future trends," *Journal of Physics: Conference Series*, vol. 1913, no. 1, p. 012053, may 2021. [Online]. Available: https://dx.doi.org/10.1088/1742-6596/1913/1/012053
- [2] M. M. Hasan, S. Hossain, M. Mofijur, Z. Kabir, I. A. Badruddin, T. M. Yunus Khan, and E. Jassim, "Harnessing solar power: A review of photovoltaic innovations, solar thermal systems, and the dawn of energy storage solutions," *Energies*, vol. 16, no. 18, 2023. [Online]. Available: https://www.mdpi.com/1996-1073/16/18/6456
- [3] J. Ma, H. Bai, W. Zhao, Y. Yuan, and K. Zhang, "High efficiency graphene/mos2/si schottky barrier solar cells using layer-controlled mos2 films," *Solar Energy*, vol. 160, pp. 76–84, 2018. [Online]. Available: https://www.sciencedirect.com/science/article/pii/S0038092X17310599
- [4] Y. Liu and F. Gu, "A wafer-scale synthesis of monolayer mos2 and their field-effect transistors toward practical applications," *Nanoscale Adv.*, vol. 3, pp. 2117–2138, 2021. [Online]. Available: http://dx.doi.org/10.1039/D0NA01043J
- [5] P. P. Singh, S. Sinha, G. Pandey, and V. Srivastava, "Molybdenum disulfide (mos2) based photoredox catalysis in chemical transformations," *RSC Adv.*, vol. 12, pp. 29 826–29 839, 2022. [Online]. Available: http://dx.doi.org/10.1039/D2RA05695J
- [6] P. Wang, S. Lin, G. Ding, X. Li, Z. Wu, S. Zhang, Z. Xu, S. Xu, Y. Lu, W. Xu, and Z. Zheng, "Enhanced monolayer mos2/inp heterostructure solar cells by graphene quantum dots," *Applied Physics Letters*, vol. 108, no. 16, p. 163901, 04 2016. [Online]. Available: https://doi.org/10.1063/1.4946856
- [7] P. K. Nayak, S. Mahesh, H. J. Snaith, and D. Cahen, "Photovoltaic solar cell technologies: analysing the state of the art," *Nature Reviews Materials*, vol. 4, pp. 269–285, 2019.

- [8] N. Shah, A. A. Shah, P. K. Leung, S. Khan, K. Sun, X. Zhu, and Q. Liao, "A review of third generation solar cells," *Processes*, vol. 11, no. 6, 2023. [Online]. Available: https://www.mdpi.com/2227-9717/11/6/1852
- [9] T. Silva, U. Arachchige, C. Kumaragamage, and V. Perera, "Solar energy technologies: A complete review of the solar system technologies," pp. 84–111, 01 2024.
- [10] R. Eke, T. Betts, and G. R., "Spectral irradiance effects on the outdoor performance of photovoltaic modules," *Renewable and Sustainable Energy Reviews*, vol. 69, pp. 429–434, 2017. [Online]. Available: https://www.sciencedirect.com/science/article/pii/S1364032116307079
- [11] P. P. Kumavat, P. Sonar, and D. S. Dalal, "An overview on basics of organic and dye sensitized solar cells, their mechanism and recent improvements," *Renewable and Sustainable Energy Reviews*, vol. 78, pp. 1262–1287, 2017. [Online]. Available: https://www.sciencedirect.com/science/article/pii/S1364032117306457
- [12] S. Bhatia, "1 energy resources and their utilisation," in *Advanced Renewable Energy Systems*, S. Bhatia, Ed. Woodhead Publishing India, 2014, pp. 1–31. [Online]. Available: https://www.sciencedirect.com/science/article/pii/B9781782422693500012
- [13] J.-M. Nunzi and B. Lavoisier, "Organic materials and devices for photovoltaic applications," 01 2002.
- [14] A. S. Al-Ezzi and M. N. M. Ansari, "Photovoltaic solar cells: A review," *Applied System Innovation*, vol. 5, no. 4, 2022. [Online]. Available: https://www.mdpi.com/2571-5577/5/4/67
- [15] M. A. Rahman, "A review on semiconductors including applications and temperature effects in semiconductors," *American Scientific Research Journal for Engineering, Technology, and Sciences (ASRJETS)*, vol. 7, no. 1, pp. 50–70, 2014.
- [16] R.Boumaraf, "Simulation de l'effet de la température et les défauts sur les caractéristiques électriques des diodes à base de gaas."
- [17] C. Pinho Correia Valério Bernardo, R. Lameirinhas, J. Cunha, and J. Torres, "A revision of the semiconductor theory from history to applications," *Discover Applied Sciences*, vol. 6, 06 2024.
- [18] F. Wang, X.-K. Liu, and F. Gao, Fundamentals of Solar Cells and Light-Emitting Diodes, 01 2019, pp. 1–35.
- [19] A. Eldakhakhny, Solar cells, 06 2020.

- [20] B. Nasir, Power Electronics, 01 2021.
- [21] N. Guerra, M. Guevara, C. Palacios, and F. Crupi, "Operation and physics of photovoltaic solar cells: an overview," *I+D Tecnológico*, vol. 14, no. 2, pp. 84–95, 2018.
- [22] R. B. Kodati and N. R. Puli, "A review of solar cell fundamentals and technologies," *Advanced Science Letters*, vol. 26, p. 260, 09 2020.
- [23] S. Arumugam, P. Murugesan, A. K. P., S. Satyanarayna, and K. Suraj, "Plasma–metal junction," *Physics of Plasmas*, vol. 27, p. 023512, 02 2020.
- [24] D. Rusirawan and I. Farkas, "Identification of model parameters of the photovoltaic solar cells," *Energy Procedia*, vol. 57, pp. 39–46, 2014, 2013 ISES Solar World Congress. [Online]. Available: https://www.sciencedirect.com/science/article/pii/S1876610214013733
- [25] K. Bouzidi, M. Chegaar, and M. Aillerie, "Solar cells parameters evaluation from dark i-v characteristics," *Energy Procedia*, vol. 18, pp. 1601–1610, 2012, terragreen 2012: Clean Energy Solutions for Sustainable Environment (CESSE). [Online]. Available: https://www.sciencedirect.com/science/article/pii/S1876610212010314
- [26] M. El-Ahmar, A.-H. Ahmed, and A. Hemeida, "Mathematical modeling of photo-voltaic module and evaluate the effect of varoius parameters on its performance," 12 2016, pp. 741–746.
- [27] M. Uddin, "Performance of different dc/dc converters for maximum power point tracking in photovoltaic systems," Ph.D. dissertation, 10 2014.
- [28] R. A. Marques Lameirinhas, J. P. N. Torres, and J. P. de Melo Cunha, "A photovoltaic technology review: History, fundamentals and applications," *Energies*, vol. 15, no. 5, 2022. [Online]. Available: https://www.mdpi.com/1996-1073/15/5/1823
- [29] J. Pastuszak and P. Węgierek, "Photovoltaic cell generations and current research directions for their development," *Materials*, vol. 15, 08 2022.
- [30] J. Jean, P. Brown, R. Jaffe, T. Buonassisi, and V. Bulovic, "Pathways for solar photovoltaics," *Energy Environ. Sci.*, vol. 8, p. 1200, 02 2015.
- [31] F. Wang, X.-K. Liu, and F. Gao, Materials for Photovoltaics: Overview, Generations, Recent Advancements and Future Prospects, 01 2019, pp. 1–35.

- [32] S. V. S. Prasad, R. K. Mishra, S. Gupta, S. B. Prasad, and S. Singh, *Introduction, History, and Origin of Two Dimensional (2D) Materials*. Singapore: Springer Singapore, 2021, pp. 1–9.
- [33] M. M. Uddin, M. H. Kabir, M. A. Ali, M. M. Hossain, M. U. Khandaker, S. Mandal, A. Arifutzzaman, t. G.-l. e. D. m. r. p. c. Jana, Debnarayan", and future outlook, "Graphene-like emerging 2d materials: recent progress, challenges and future outlook," *RSC Adv.*, vol. 13, pp. 33336–33375, 2023. [Online]. Available: http://dx.doi.org/10.1039/D3RA04456D
- [34] O. S. Omar, "Monolayer mos2/n-si heterostructure schottky solar cell," *Journal of Renewable Materials*, vol. 10, no. 7, 2022.
- [35] R. Mas-Ballesté, C. Navarro, J. Gómez-Herrero, and F. Zamora, "2d materials: To graphene and beyond," *Nanoscale*, vol. 3, pp. 20–30, 01 2011.
- [36] Y. Lei, T. Zhang, Y.-C. Lin, T. Granzier-Nakajima, G. Bepete, D. A. Kowalczyk, Z. Lin, D. Zhou, T. F. Schranghamer, A. Dodda, A. Sebastian, Y. Chen, Y. Liu, G. Pourtois, T. J. Kempa, B. Schuler, M. T. Edmonds, S. Y. Quek, U. Wurstbauer, S. M. Wu, N. R. Glavin, S. Das, S. P. Dash, J. M. Redwing, J. A. Robinson, and M. Terrones, "Graphene and beyond: Recent advances in two-dimensional materials synthesis, properties, and devices," *ACS Nanoscience Au*, vol. 2, no. 6, pp. 450–485, 2022. [Online]. Available: https://doi.org/10.1021/acsnanoscienceau.2c00017
- [37] M. Srivastava, S. Banerjee, S. Bairagi, P. Singh, B. Kumar, P. Singh, R. D. Kale, D. M. Mulvihill, and S. W. Ali, "Recent progress in molybdenum disulfide (mos2) based flexible nanogenerators: An inclusive review," *Chemical Engineering Journal*, vol. 480, p. 147963, 2024. [Online]. Available: https://www.sciencedirect.com/science/article/pii/S1385894723066950
- [38] H. Xu, J. Zhu, Q. Ma, J. Ma, H. Bai, L. Chen, and S. Mu, "Two-dimensional mos2: Structural properties, synthesis methods, and regulation strategies toward oxygen reduction," *Micromachines*, vol. 12, no. 3, 2021. [Online]. Available: https://www.mdpi.com/2072-666X/12/3/240
- [39] K. M. H. Ismail, M. A. Kumar, S. Mahalingam, J. Kim, and R. Atchudan, "Recent advances in molybdenum disulfide and its nanocomposites for energy applications: Challenges and development," *Materials*, vol. 16, 2023. [Online]. Available: https://api.semanticscholar.org/CorpusID:259228904

- [40] O. Samy, S. Zeng, M. D. Birowosuto, and A. El Moutaouakil, "A review on mos2 properties, synthesis, sensing applications and challenges," *Crystals*, vol. 11, no. 4, 2021. [Online]. Available: https://www.mdpi.com/2073-4352/11/4/355
- [41] X. Li and H. Zhu, "Two-dimensional mos2: Properties, preparation, and applications," *Journal of Materiomics*, vol. 1, no. 1, pp. 33–44, 2015. [Online]. Available: https://www.sciencedirect.com/science/article/pii/S2352847815000040
- [42] M.-h. Wu, L. Li, N. Liu, D.-j. Wang, Y.-c. Xue, and L. Tang, "Molybdenum disulfide (mos 2) as a co-catalyst for photocatalytic degradation of organic contaminants: A review," *Process Safety and Environmental Protection*, vol. 118, 06 2018.
- [43] M. Saliba, J. P. Atanas, T. M. Howayek, and R. Habchi, "Molybdenum disulfide, exfoliation methods and applications to photocatalysis: a review," *Nanoscale Adv.*, vol. 5, pp. 6787–6803, 2023. [Online]. Available: http://dx.doi.org/10.1039/D3NA00741C
- [44] M. S. Ullah, A. H. B. Yousuf, A. D. Es-Sakhi, and M. H. Chowdhury, "Analysis of optical and electronic properties of mos2 for optoelectronics and fet applications," *AIP Conference Proceedings*, vol. 1957, no. 1, p. 020001, 04 2018. [Online]. Available: https://doi.org/10.1063/1.5034320
- [45] K. Islam, R. Synowicki, T. Ismael, I. Oguntoye, N. Grinalds, and M. Escarra, "Inplane and out-of-plane optical properties of monolayer, few-layer, and thin-film mos2 from 190 to 1700 nm and their application in photonic device design," *Advanced Photonics Research*, vol. 2, 03 2021.
- [46] S. Ahmad and S. Mukherjee, "A comparative study of electronic properties of bulk mos2 and its monolayer using dft technique: Application of mechanical strain on mos2 monolayer," *Graphene*, vol. 03, pp. 52–59, 01 2014.
- [47] N. Thomas, S. Mathew, K. Nair, K. O'Dowd, P. Forouzandeh, A. Goswami, G. McGranaghan, and S. Pillai, "2d mos2: structure, mechanisms, and photocatalytic applications," *Materials Today Sustainability*, vol. 13, p. 100073, 2021. [Online]. Available: https://www.sciencedirect.com/science/article/pii/S2589234721000142
- [48] S. Ansari, R. Kumar, M. Barakat, and M. H. Cho, "Simple and sustainable route for large scale fabrication of few layered molybdenum disulfide sheets towards superior adsorption of the hazardous organic pollutant," *Journal of Materials Science: Materials in Electronics*, vol. 29, 05 2018.

- [49] X. Yu, X. Wang, F. Zhou, J. Qu, and J. Song, "2d van der waals heterojunction nanophotonic devices: From fabrication to performance," *Advanced Functional Materials*, vol. 31, 07 2021.
- [50] D. Mouloua, A. Kotbi, G. Deokar, K. Kaja, M. El Marssi, M. A. EL Khakani, and M. Jouiad, "Recent progress in the synthesis of mos2 thin films for sensing, photovoltaic and plasmonic applications: A review," *Materials*, vol. 14, no. 12, 2021. [Online]. Available: https://www.mdpi.com/1996-1944/14/12/3283
- [51] S. Lin, X. Li, P. Wang, Z. Xu, S. Zhang, H. Zhong, Z. Wu, W. Xu, and H. Chen, "Interface designed mos2 /gaas heterostructure solar cell with sandwich stacked hexagonal boron nitride," *Scientific Reports*, vol. 5, p. 15103, October 2015.
- [52] M. Dey, M. Dey, S. Alam, N. Das, M. Matin, and N. Amin, "Study of molybdenum sulphide as a novel buffer layer for czts solar cells," 09 2016, pp. 1–4.
- [53] O. Samy and A. El Moutaouakil, "A review on mos2 energy applications: Recent developments and challenges," *Energies*, vol. 14, no. 15, 2021. [Online]. Available: https://www.mdpi.com/1996-1073/14/15/4586
- [54] H. Xu, L. Xin, L. Liu, D. Pang, Y. Jiao, R. Cong, and W. Yu, "Large area mos2/si heterojunction-based solar cell through sol-gel method," *Materials Letters*, vol. 238, pp. 13–16, 2019. [Online]. Available: https://www.sciencedirect.com/science/article/pii/S0167577X18318111
- [55] F. Zafar and A. Iqbal, "Indium phosphide nanowires and their applications in optoelectronic devices," *Proceedings of the Royal Society A: Mathematical, Physical and Engineering Sciences*, vol. 472, no. 2187, p. 20150804, 2016. [Online]. Available: https://royalsocietypublishing.org/doi/abs/10.1098/rspa.2015.0804
- [56] G. R. Patzke, R. Kontic, Z. Shiolashvili, N. Makhatadze, and D. Jishiashvili, "Hydrazine-assisted formation of indium phosphide (inp)-based nanowires and core-shell composites," *Materials*, vol. 6, no. 1, pp. 85–100, 2013. [Online]. Available: https://www.mdpi.com/1996-1944/6/1/85
- [57] M. Salman, A. Ullah, S. Zaman, E. Mahmoud, and M. Belay, "3d molecular structural modeling and characterization of indium phosphide via irregularity topological indices," *BMC Chemistry*, vol. 18, p. 101, 05 2024.
- [58] R. Fornari, "Indium phosphide," in *Encyclopedia of Materials: Science and Technology*, K. J. Buschow, R. W. Cahn, M. C. Flemings, B. Ilschner, E. J. Kramer, S. Mahajan, and P. Veyssière, Eds. Oxford: Elsevier, 2001, pp. 4061–4065. [Online]. Available: https://www.sciencedirect.com/science/article/pii/B0080431526007129

- [59] W. Hui, L. Sherin, S. Javed, S. Khalid, W. Asghar, and S. A. Fufa, "On topological indices for complex indium phosphate network and their applications," *Complexity*, vol. 2022, pp. 1–17, 01 2022.
- [60] C. D. Vedel, S. Smidstrup, and V. P. Georgiev, "First-principles investigation of polytypic defects in inp," *Scientific Reports*, vol. 12, p. 19724, 2022.
- [61] S. Datta, T. Saha-Dasgupta, and D. Sarma, "Wannier function study of the relative stability of zinc-blende and wurtzite structures in the cdx (x = s, se, te) series," *Journal of Physics: Condensed Matter*, vol. 20, p. 445217, 10 2008.
- [62] K. Kabita, J. Maibam, B. Sharma, R. Thapa, and R. K. B. Singh, "First principle study on pressure-induced electronic structure and elastic properties of indium phosphide (inp)," *Indian Journal of Physics*, vol. 89, pp. 1265–1271, 2015. [Online]. Available: https://api.semanticscholar.org/CorpusID:122557222
- [63] M. E. Levinshtein, S. L. Rumyantsev, and M. Shur, Eds., *Handbook Series on Semi-conductor Parameters. Volume 1, Si, Ge, C (diamond), GaAs, GaP, GaSb, InAs, InP, InSb.* Singapore: World Scientific, 1996.
- [64] S. Ehsanfar, F. Kanjouri, H. Tashakori, and A. Esmailian, "First-principles study of structural, electronic, mechanical, thermal, and phonon properties of iii-phosphides (bp, alp, gap, and inp)," *Journal of Electronic Materials*, vol. 46, 06 2017.
- [65] B. Ali, T. Ouahrani, M. Ameri, R. Mebsout, and D. Hachemane, "Theoretical study of structural, electronic, optical and thermodynamic properties of aip, inp and alas compounds," *Journal of Optoelectronics and Advanced Materials*, vol. 710, pp. 659–666, 10 2012.
- [66] D. E. Aspnes and A. A. Studna, "Dielectric functions and optical parameters of si, ge, gap, gaas, gasb, inp, inas, and insb from 1.5 to 6.0 ev," *Phys. Rev. B*, vol. 27, pp. 985–1009, Jan 1983. [Online]. Available: https://link.aps.org/doi/10.1103/PhysRevB.27.985
- [67] M. Altamirano-Lozano, D. Beyersmann, D. Carter, B. Fowler, B. Fubini, J. Kielhorn, M. Kirsch-Volders, J. Kucera, Y. Kusaka, G. Lasfargues, D. Lison, I. Mangelsdor, D. McElvenny, B. Nemery, J. Roycroft, M. Svartengren, T. Junghans, S. Olin, R. Renne, D. Longfellow, K. Ziegler-Skylakakis, R. Baan, V. Cogliano, F. El Ghissassi, T. Fletcher, M. Friesen, Y. Grosse, N. Napalkov, B. Secretan, K. Straif, Z. Wang, and R. Williams", ""cobalt in hard metals and cobalt sulfate, gallium arsenide, indium phosphide and vanadium pentoxide"," in Cobalt in Hard Metals and Cobalt Sulfate, Gallium Arsenide, Indium Phosphide and Vanadium Pentox-

- *ide*, ser. IARC Monographs on the Evaluation of Carcinogenic Risks to Humans, A. Thomas, M. Altamirano-Lozano, and D. Beyersmann, Eds., "2006", pp. i–292.
- [68] T. Inada, T. Fujii, M. Eguchi, and T. Fukuda, "Technique for the direct synthesis and growth of indium phosphide by the liquid phosphorus encapsulated czochralski method," *Applied Physics Letters*, vol. 50, no. 2, pp. 86–88, 01 1987. [Online]. Available: https://doi.org/10.1063/1.97827
- [69] T. Inada and T. Fukuda, "Chapter 3 direct synthesis and growth of indium phosphide by the liquid phosphorus encapsulated czochralski method," ser. Semiconductors and Semimetals, R. Willardson and A. C. Beer, Eds. Elsevier, 1990, vol. 31, pp. 71–92. [Online]. Available: https://www.sciencedirect.com/science/article/pii/S0080878408625557
- [70] D. H. Choi, J. H. Lee, M. S. Kim, J. Park, J. O. Kim, T. A. Mahadev, B. S. Ajay, H. H. Kim, and J. C. Shin, "Wet-transferred mos2 on passivated inp: A van der waals heterostructure for advanced optoelectronic applications," *physica status solidi (RRL) Rapid Research Letters*, vol. 19, no. 5, p. 2500001, 2025. [Online]. Available: https://onlinelibrary.wiley.com/doi/abs/10.1002/pssr.202500001
- [71] S. Lin, P. Wang, X. Li, Z. Wu, Z. Xu, S. Zhang, and W. Xu, "Gate tunable monolayer mos2/inp heterostructure solar cells," *Applied Physics Letters*, vol. 107, no. 15, p. 153904, 10 2015. [Online]. Available: https://doi.org/10.1063/1.4933294
- [72] N. Khadidja, "Simulation of cuprous oxide solar cells using silvaco tcad."
- [73] E. Mourad, "Etude par simulation numérique d'une cellule solaire en cigs à multijonction par le logiciel tcad silvaco."
- [74] N. E. I. Boukortt, "Study and simulation of a nanoscale structure of a multi-gate mos transistor," PhD thesis, Università degli Studi di Messina and Università di Mostaganem, 2016.
- [75] M. N. Kateb, "Étude par simulation numérique d'une cellule solaire en a-si:h/µc-si:h multijonction."
- [76] Y.-H. Lee, X.-Q. Zhang, W. Zhang, M.-T. Chang, C.-T. Lin, K.-D. Chang, Y.-C. Yu, J. T.-W. Wang, C.-S. Chang, L.-J. Li, and T.-W. Lin, "Synthesis of large-area mos2 atomic layers with chemical vapor deposition," *Advanced Materials*, vol. 24, no. 17, pp. 2320–2325, 2012. [Online]. Available: https://advanced.onlinelibrary.wiley.com/doi/abs/10.1002/adma.201104798
- [77] N. Huo, Y. Yang, Y.-N. Wu, X.-G. Zhang, S. T. Pantelides, and G. Konstantatos, "High carrier mobility in monolayer cvd-grown mos2 through phonon

- suppression," *Nanoscale*, vol. 10, pp. 15071–15077, 2018. [Online]. Available: http://dx.doi.org/10.1039/C8NR04416C
- [78] C. Wang, L. Cusin, C. Ma, E. Unsal, H. Wang, V. G. Consolaro, V. Montes-García, B. Han, S. Vitale, A. Dianat, A. Croy, H. Zhang, R. Gutierrez, G. Cuniberti, Z. Liu, L. Chi, A. Ciesielski, and P. Samorì, "Enhancing the carrier transport in monolayer mos2 through interlayer coupling with 2d covalent organic frameworks," *Advanced Materials*, vol. 36, no. 1, p. 2305882, 2024. [Online]. Available: https://advanced.onlinelibrary.wiley.com/doi/abs/10.1002/adma.202305882
- [79] C. Hsu, J. Yuan, R. Cohen, and G. Stringfellow, "Doping studies for inp grown by organometallic vapor phase epitaxy," *Journal of Crystal Growth*, vol. 74, no. 3, pp. 535–542, 1986. [Online]. Available: https://www.sciencedirect.com/science/article/pii/0022024886901995
- [80] B. Chakraborty, A. Bera, D. V. S. Muthu, S. Bhowmick, U. V. Waghmare, and A. K. Sood, "Symmetry-dependent phonon renormalization in monolayer mos₂ transistor," *Phys. Rev. B*, vol. 85, p. 161403, Apr 2012. [Online]. Available: https://link.aps.org/doi/10.1103/PhysRevB.85.161403
- [81] N. Lu, H. Guo, L. Li, J. Dai, L. Wang, W.-N. Mei, X. Wu, and X. C. Zeng, "Mos2/mx2 heterobilayers: bandgap engineering via tensile strain or external electrical field," *Nanoscale*, vol. 6, pp. 2879–2886, 2014. [Online]. Available: http://dx.doi.org/10.1039/C3NR06072A
- [82] K. F. Mak, C. Lee, J. Hone, J. Shan, and T. F. Heinz, "Atomically thin mos₂: A new direct-gap semiconductor," *Phys. Rev. Lett.*, vol. 105, p. 136805, Sep 2010. [Online]. Available: https://link.aps.org/doi/10.1103/PhysRevLett.105.136805
- [83] B. Ofuonye, J. Lee, M. Yan, C. Sun, J.-M. Zuo, and I. Adesida, "Electrical and microstructural properties of thermally annealed ni/au and ni/pt/au schottky contacts on algan/gan heterostructures," *Semiconductor Science and Technology*, vol. 29, p. 095005, 07 2014.
- [84] M. Stössel, J. Staudigel, F. Steuber, J. Simmerer, and A. Winnacker, "Impact of the cathode metal work function on the performance of vacuum-deposited organic light emitting-devices," *Applied Physics A*, vol. 68, pp. 387–390, 04 1999.

REPUBLIQUE ALGERIENNE DEMOCRATIQUE ET POPULAIRE MINISTERE DE L'ENSEIGNEMENT SUPERIEUR ET DE LA RECHIERCHE SCIENTIFIQUE UNIVERSITE MOHAMED KHIDER - BISKRA



الجمهورية الجزئرية الديمقراطية الثعبية وزارة التعليم العالي والبحث العلمي جامعة محرى؛ خيرضر يسركرة مُعُلِمة العلوم الدنيفة

Faculté des SE

Département des Sciences de la matière

Filière: Physique

قسم علوم المادة

شعبة :الفيزياء

تصريح شرفسي

ص بالالتزام بقواعد النزاهة العلمية لإنجاز بحث

(ملحق القرار 1082 المؤرخ في 2021/12/27)

انا المعضى اسفله،

السيد(ة) ... إ حسمان بين عمر سور

تخصص العبر المراب المراب

أصرح بشرفي أني ألتزم بمراعاة المعايير العلمية والمنهجية ومعايير الأخلاقيات المهنية والنزاهة الأكاديمية المطلوبة في انجاز البحث المذكور أعلاه وفق ما ينص عليه القرار رقم 1082 المؤرخ في 2021/1022 المدورخ في المدادد للقواعد المتعلقة بالوقاية من السرقة العلمية ومكافحتها.

التاريخ:

امضاء المعنى بالأمر

8